The Impact of Reservoir Heterogeneity on CO$_2$ Capture and Storage

Analyzing the effect of sedimentological heterogeneity in a reservoir inspired by Sobrarbe deltaic complex on CO$_2$ Storage using RRM and CMG

Abdullrhman Abdullah Alkhunaini

TUDelft

The Impact of Reservoir Heterogeneity on CO_2 Capture and Storage

Analyzing the effect of sedimentological heterogeneity in a reservoir inspired by Sobrarbe deltaic complex on CO_2 Storage using RRM and CMG

Thesis report

by

Abdullrhman Abdullah Alkhunaini

to obtain the degree of Master of Science
at the Delft University of Technology
to be defended publicly on September 15, 2024

Thesis committee:

Chair:	Associate professor Dr.Joep Storms
Supervisors:	Prof.Dr. S. (Sebastian) Geiger
	Assistant professor Dr. Alexandros Daniilidis
Student number:	5745187

An electronic version of this thesis is available at `http://repository.tudelft.nl/`.

Faculty of Civil Engineering and Geosciences · Delft University of Technology

TU Delft

Delft
University of
Technology

Abstract

CO_2 emissions are a major driver of global warming, contributing significantly to the level of climate change. One promising solution to mitigate this issue is Carbon Capture and Storage, which involves capturing CO_2 emissions from industrial sources and securely storing them in reservoirs or aquifers. The study investigates the impact of large-scale reservoir heterogeneity on the efficiency of the CO_2 storage by using reservoir models inspired by the Sobrarbe Deltaic Complex outcrop in Ainsa, Spain. Utilizing Google Earth, RRM (Rapid Reservoir Modeling), and CMG software, different reservoir realizations were created, incorporating various levels of petrophysical properties and impermeable layers within the reservoir. The models simulated 100 years of CO_2 injection and monitoring. Results indicate that the Base Model, characterized by continuous impermeable layers and high porosity and permeability values, represented the highest cumulative trapped CO_2, capturing approximately 3 billion kg of CO_2. Models with patchy impermeable layers and lower petrophysical properties values represented lower CO_2 trapping efficiency. The results highlight the critical role of reservoir heterogeneity in determining the storage potential and pressure stability of CO_2 storage projects, offering valuable insight into the feasibility of carbon storage initiatives.

Acknowledgement

I would like to express my deepest gratitude to everyone who supported me throughout the completion of this thesis.

First and foremost, I would like to extend my heartfelt thanks to Dr. Joep Storms, my thesis chair. His exceptional expertise and insightful feedback provided me with valuable guidance throughout this research. Dr. Storms' deep understanding of the subject and his ability to challenge my thinking helped me refine my work and approach problems from new perspectives. His unwavering support and encouragement were instrumental in shaping the direction and quality of this thesis.

I am also incredibly thankful to my thesis supervisors, Prof. Dr. Sebastian Geiger and Dr. Alexandros Daniilidis, for their continuous guidance and valuable insights. Their expertise and advice have been essential in guiding this work, and I deeply appreciate the time and effort they invested in helping me succeed.

A special mention goes to my colleagues and fellow students at Delft University of Technology, who provided me with moral support and shared their experiences and knowledge throughout this journey. Their support and collaboration made this experience both rewarding and enjoyable.

To my family, I owe my deepest gratitude. To my parents, thank you for your unconditional love, support, and belief in me. Your strength has been my foundation. To my brothers and sisters, your constant encouragement has kept me going through challenging times.

To my wonderful wife, Aseel, who was pregnant during this journey, your patience and support have been a source of strength for me. Thank you for standing by me through it all. To my beautiful daughter, Salma, who was born at the beginning of this program, you made things a little more challenging, but your presence has been my greatest motivation. Though I couldn't always be with you, you were always in my heart, and every step of this progress was inspired by you.

Thank you all for making this achievement possible.

Contents

List of Figures

List of Tables

1

Introduction

The CO_2 emission in the atmosphere is one of the main threats to the sustainability of our environment. As a Saudi citizen working for the largest oil and gas company, the responsibilities are higher and require creative approaches to reach the goal of Saudi green initiatives of zero carbon emissions in 2060 [1]. For that, carbon capture and storage can be a major factor in maintaining the Paris Climate Agreement, [2], and ensuring a sustainable environment for future generations. The challenge of the carbon storage technique is identifying reservoirs or aquifers that can accommodate the CO_2 volume and assess the heterogeneity of these reservoirs and their effect on injected CO_2. In this report, a reservoir model inspired by the outcrop of the Sobrarbe deltaic complex in Spain is chosen to conduct an analysis including medium to large-scale heterogeneity that can be reflected in CO_2 storage application. The Sobrarbe deltaic complex vertically extends to three formations (Sobrarbe Formation, Escanilla Formation, and San Vicente Formation) that outcropped in the western side of the Eocene Ainsa basin [3]. The Sobrarbe deltaic complex can be subdivided into five main composite sequences and five facies associations representing depositional environments from shelf to distal slope [4]. The trapping of CO_2 in the reservoir is mainly dominated by structural and stratigraphic mechanisms within a short time scale, around 100 years. Then, the influence of other types of trapping mechanisms increases such as residual CO_2 and solubility. Around 1000 to 10,000 years, all trapping mechanisms have approximately similar impact [5]. The main focus of this study is analyzing the short time scale "100 years" of injection and monitoring of CO_2 considering structural and stratigraphic trapping and residual trapping as illustrated in figure 1.1.
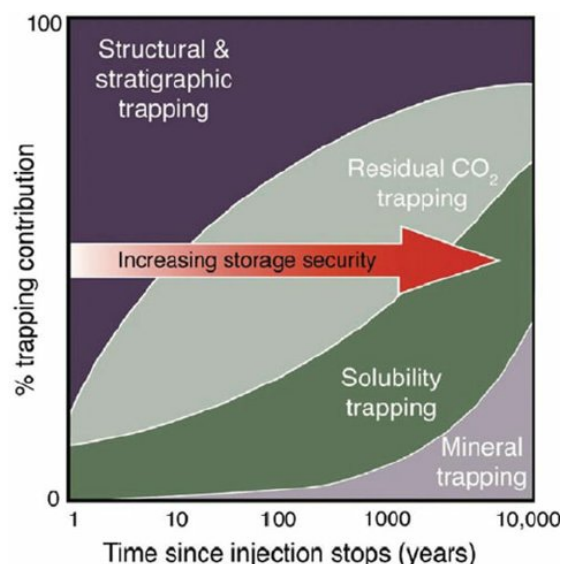
Figure 1.1: The CO_2 trapping mechanism a long period of time [6]

1

1.1. Research Question:

Main question:
How do reservoir architecture and large-scale heterogeneities (ranging from tens of meters to hundreds of meters in vertical and lateral extent) in a reservoir inspired by the Sobrarbe Deltaic Complex outcrop influence the CO_2 migration plume, injection rates, and total amount of injected/stored CO_2 volume within a time scale 50 years of injection and 50 years of monitoring?

Sub-questions:
- How does the CO_2 plume behave with different reservoir scenarios based on different porosity and permeability values?

- How does the lateral continuity of facies within the reservoir affect the CO_2 plume movement, injection rates, and total amount of injected/stored CO_2 volume?

- Which reservoir scenario shows the higher efficiency in accommodating CO_2?

To answer these questions, the study has the following objectives: construct a geological model that captures the heterogeneity and reservoir architecture at the facies association level inspired by the Sobrarbe Deltaci Complex outcrop. Introducing different realizations for the geological model reservoir by having high setting and low setting for both heterogeneity and reservoir architecture. Then, simulating the static models using CMG software for CO_2 application to conduct the analysis.

<div align="right">

2

</div>

Geological Setting of Ainsa Basin

2.1. Structural Settings

The Pyrenean Central Thrust Systems orogeny is due to the convergence between the Iberian micro-plate and the Eurasian plate. Along with the convergence, subduction of the Iberian Plate created a thrust belt and asymmetric fold from the late Cretaceous to Miocene periods [7] and [8]. The faults inversion within the rift basin in Mesozoic time is due to the Pyrenees uplift, which led to the formation of the South Pyrenean Foreland basin and North Aquitanian basin [9]. In the Pyrenean Foreland basin, other basins formed in the thrust sheet such as the Ainsa basin, Jaca basin, and Tremp-Graus basin [10]. The South Pyrenean Central Thrust System consists of three thrust systems: lower thrust system, middle thrust system, and upper thrust system, which create a piggy-back system in the Eocene. Within the three thrust systems, Ainsa Basin is located in the upper part and also part of a larger scale piggy-back basin, which is Tremp-Ainsa Jaca piggy-back as illustrated in figure 2.1 [7]. The Ainsa Basin is formed within the upper Maastrichtian to Paleocene in the South Pyrenean Central Thrust System, as illustrated in figure 2.1. During that period, the inversion of the basin was the dominant cause of deformation in the Ainsa Basin and South Pyrenean Central Thrust System. Then, between the Early Eocene to the Middle Eocene, the thrusting along north to south of the axial zone started to become dominant [11].
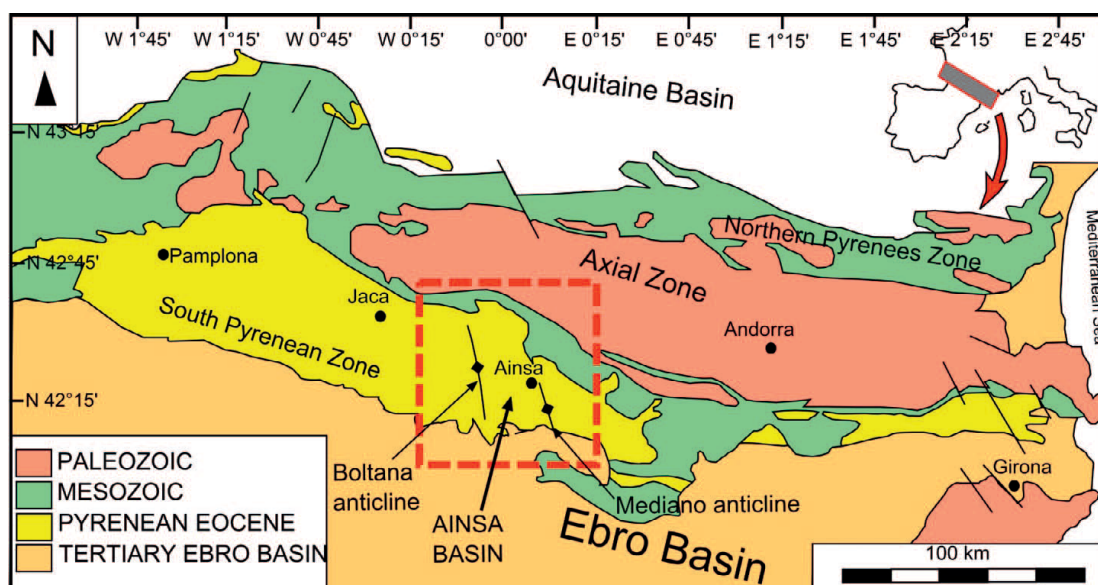
Figure 2.1: A map illustrating several thrust sheets within the Pyrenean zones, Ainsa Basin in the middle, and Jaca in the west of the map. The color legend indicates the time creation [12]

The Ainsa Basin extension is 6 km along the E-W direction and 12 km along N-S direction [12]. In addition, the structural boundary of Ainsa Basin is illustrated as the following: west is Boltana Anticline,

<div align="center">

3

</div>

the Median Anticline in the east, the Anisclo Anticline in the north, the Cotiella thrust in the northwest and the Montsec thrust in the south [7]. Both Boltana Anticline and Median Anticline are considered transport-oblique thrust ramps [13]. The Ainsa Basin development started at the Cuisian-Lutetian transition as the bounded area was subjected to subsidence, above the South Pyrenean Central Thrust an accumulation of both deltaic and continental deposits represented by Tremp-Graus piggy-back [13].

In the early Lutetian, the Sobrarbe Deltaic Complex was formed within two basins: the Tremp-Graus basin (alluvial zone) and the Jaca basin (basin zone). The Mediano anticline in the early Lutetian was causing a slope for sediment supply into the Ainsa basin [14] and [15]. In the Ainsa basin, the slope of marls and channels that formed due to turbidities are generated and delta front and delta plain are formed in the south of the Ainsa basin [16] and [17].
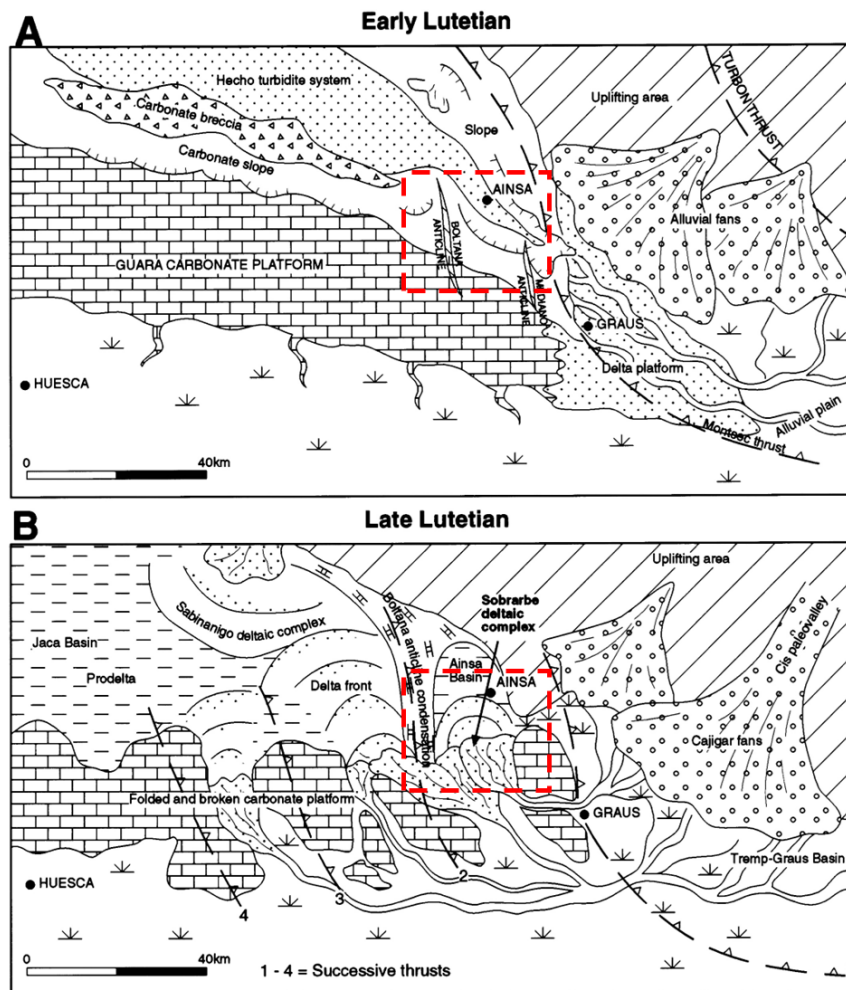
Figure 2.2: A schematic constructions for Ainsa Basin indicating the Sobrarbe deltaic complex deposition, A: Early Lutetian and B: Late Lutetian [13], the red rectangle illustrates the study area.

In the late Lutetian, the development of thrust-ramp anticlines led to the exposure of the Ainsa and Jaca basins as part of the shifting of the foreland setting. In addition, the area was subjected to uplifting that caused an increase of deltaic deposits in the south of the Jaca basin [18]. While in the Ainsa basin, the delta deposits reached the basin due to the lower slope structures that led to a change in the source direction to north-northwest [13].

2.2. Sedimentological Settings

2.2.1. Sobrarbe Deltaic Complex

The Sobrarbe Deltaic Complex deposits extend from the middle part of Mondot Member, which is part of the Escanilla Formation, Sobrarbe Formation, and the upper part of the San Vicente Formation as illustrated in figure 2.3. In general, the upper part of the San Vicente Formation is dominated by turbidite deposits and marl deposits. The Sobrarbe Formation is dominated by shallow marine deposits and the middle part of Mondot Member in Escanilla Formation is dominated by fluvial deposits. The accumulation of the Sobrarbe Deltaic Complex was within a period of 3 million years, between Lutetian to Lower Bartonian, and has a maximum thickness of 3 km [19].
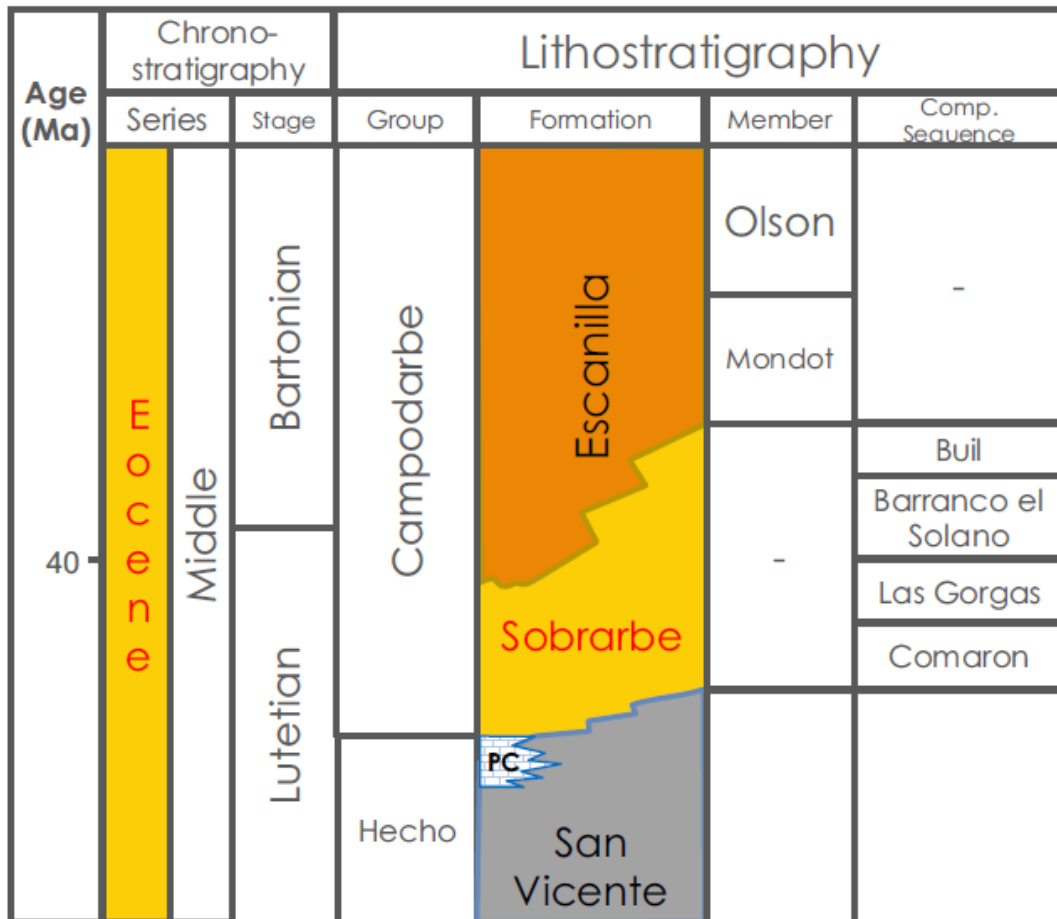
Figure 2.3: A stratigraphic unit for the Sobrarbe Deltaic Complex in Ainsa Basin. PC: Puy de Cinca Formation [20]

The Sobrarbe Deltaic Complex consists of five composite sequences bounded by unconformities. A composite sequence is composed of sets of sequences and each sequence is composed of parasequences and stacked into lowstand, transgressive, and systems tracts [21]. The composite sequences are: 1) the Comaron Composite Sequence, 2) the Las Gorgas Composite Sequence, 3) the Branco el Solano Composite Sequence, 4) the Buil Composite Sequence, and 5) the Mondot Composite Sequence. In each composite sequence, prograding clinoforms vary in terms of size within all composite sequences [7]. The Comaron Composite Sequence consists of six sequences and these sequences represent wedges of sandstone with a progradation toward the basin, each wedge is bounded by mudstone from a transgressive event. As the development of the Boltana and Arcusa anticline, a folding of the Comaron Composite Sequence led to a shift in the sandstone wedge to north-south and a trend of thinning of the beds toward the top of the anticline representing the Las Gorgas Composite Sequence. The boundary between the

Las Gorgas Composite Sequence and the Branco el Solano Composite Sequence indicates regional reconstructions of the delta front in the Sobrabre Deltaic Complex due to tectonic deformation.

Globally, the climate change transition from warm to cold phase was observed between the Eocene to Oligocene series. The palaeoclimate in the Pyrenees Central was characterized by warm and dry during the early stages of Eocene. In the middle of the Eocene, the Pyrenees were exposed to tropical to subtropical climate, which led to the development of nummulite banks. In the early stage of the Oligocene, the glaciation in the Antarctic led to a paleoclimate of colder and arid conditions [22].

2.2.2. Depostional Environment of Sobrarbe Deltaic Complex

The Sobrarbe Formation is considered the latest marine deposits in the Ainsa Basin. The age of deposition is between the upper and middle of Lutetian and the sources of deposition of the Sobrarbe Formation are the Pyrenean massif and Tremp-Graus Basin [7]. The thickness of the Sobrarbe Formation is approximately 800 m, with deposits of conglomerates at the upper part, sandstone at the middle part, and carbonate and shaly deltaic at the base. The depositional environment of the Sobrarbe Formation is a river-dominated delta, which is subdivided into five parts as follows: upper delta plain, lower delta plain, delta front, prodelta, and alluvial deposits, as illustrated in figure 2.3 [12]. The San Vicente Formation bounds the Sobrarbe Formation at the base, where the boundary is marked by organic-rich shale representing a condensed section that is correlatable along the basin. The Escanilla Formation is overlying the Sobrarbe Formation and is dominated by fluvial deposits [7].
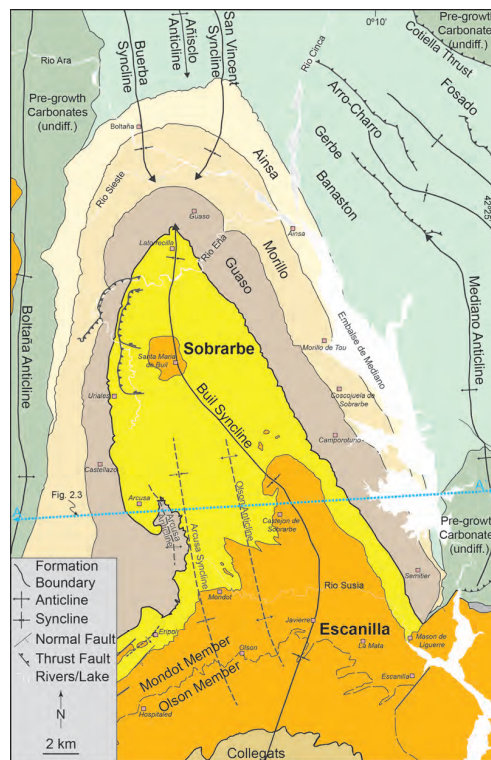
Figure 2.4: A geological map of Sobrarbe Formation, Guaso Formation, and Escanilla Formation, the boundary of the formations is marked by bold lines. Legend is provided for displayed data in the map [7]

Facies and Facies Associations of Sobrarbe Deltaic Complex:
The proposed facies and facies associations used in this project, gathered from core data and literature, represent a simplified classification as core data shows higher resolution:

Prodelta/Turbidity deposits (FA1): characterized by thin turbidites and black shale layers [22]. Figure A 2.7 shows an outcrop image of the prodelta deposits. The facies association consists of the following facies:

1. Dark shale.

2. Slump-deformed shale and sandstone.

3. Shale and very fine sandstone.

The prodelta deposits are not included in the reservoir study but are only considered potential lateral seals for the reservoir.

Delta front deposits (FA2): characterized by sandstone bodies and grey mudstone with a coarsening upward [22]. The deposit consists of the following facies:

1. Laminated very coarse-grained sandstone.

2. Laminated fine sandstone with ripples.

3. Cross-bedded-very coarse-grained sandstone.

4. Clas-supported conglomerate.

5. Grey marly siltstone.

The facies deposits form tens of meters laterally continuous sandstone packages and are bounded by erosional surfaces at the base and flooding surfaces at the top. The dominant fossils are Nummulites and echinoids [13]. Figures A, B, and C 2.7 show outcrop images of delta front deposits.

Delta plain deposits (FA3): characterized by sandstone body and conglomerate with fining-upward trend [22]. The facies association consists of the following facies:

1. Cross-bedded very coarse-grained sandstone.

2. Graded and laminated very coarse-grained sandstone.

3. Matrix-supported conglomerate.

4. Grey marly siltstone

The facies are bounded at the base by a down-dip by the delta front and an up-dip by the alluvial deposits at the top [13]. The facies association is divided into two sub-facies associations, lower delta plain and upper delta plain. The delta plain facies association is deposited in sub-aerial to sub-aqueous environments with the influence of a tidal environment [23]. Figure E 2.7 illustrates the deposits in an outcrop photograph.

To capture the transition between the fluvial deposits and the deltaic deposits, two facies associations are considered within the Delta plain deposits. The two facies association are as follows:

Shelf edge to medial slope mouth bar deposits (FA4): observed in two locations in the outcrop, location 1 and location 2 in figure 2.5. In both locations, the mouth bars are orientated parallel to the direction of sediment transport. The deposits of the mouth bar are dominated in the shelf-to-shelf edge and extend to the upper section of the slope. In the observed locations, the mouth bars are separated by surfaces characterized by an erosional base. The length of the mouth bar ranges from 1 to 2 km and the range of thickness is 40 to 50 m [24]. The dominant facies are:

1. conglomeratic sandstone.

2. Bioturbated structureless silty sandstone with bioclast.

Channel deposits (FA5): observed in two locations, location 2 and location 3 in figure 2.5. The deposits of the channel are dominated in the slope, with parallel orientation to the direction of sediment transport. The stacking pattern is vertically in the proximal part of the slope and the lateral pattern is more dominating in the distal part of the slope. The thickness of the channel ranges from 1 - 2.5m [24] and 150 m for the average width of the channel [7]. The dominant facies are:

1. Shale-clast conglomerates.

2. Clast rich sandstone.
3. Parallel to cross-laminated sandstone.
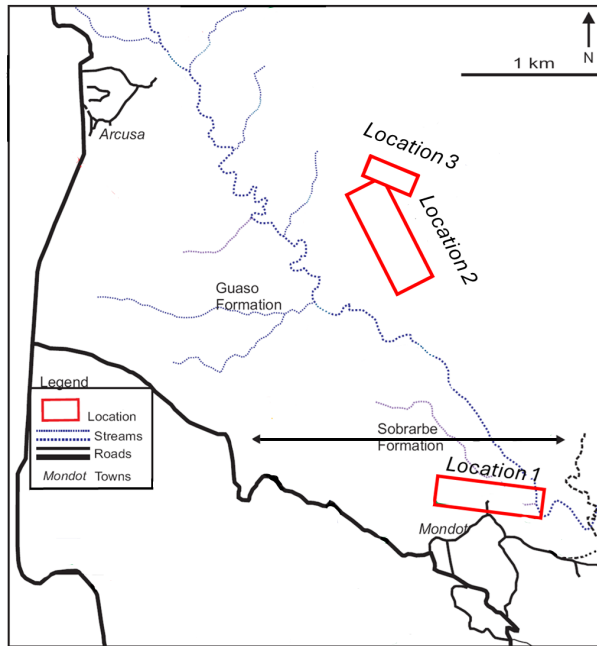
Figure 2.5: A base map illustrates the locations of mouth bar and channel deposits considered in this study, the legend is provided for roads, and streams [11]
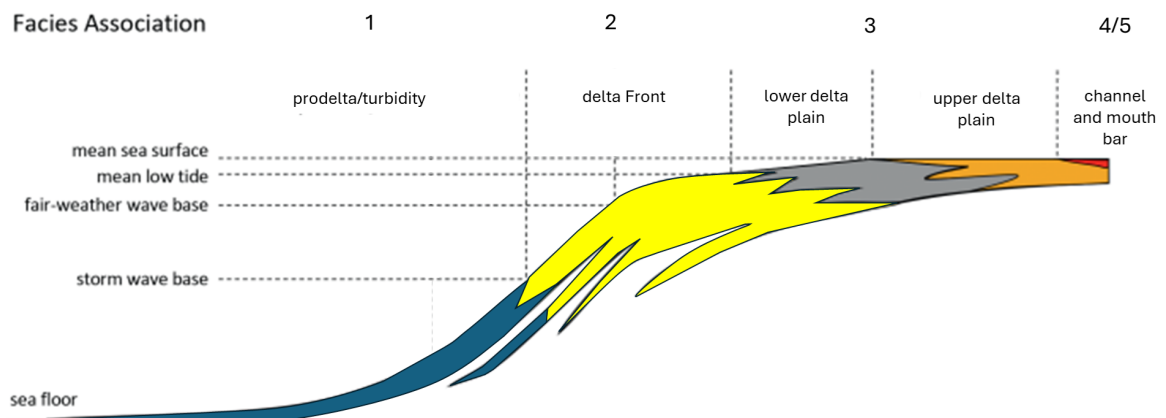
Figure 2.6: Schematic cross section for the Sobrarbe Deltaic Complex by integrating outcrop and core studies, with a sea level as a reference, modified from [25]
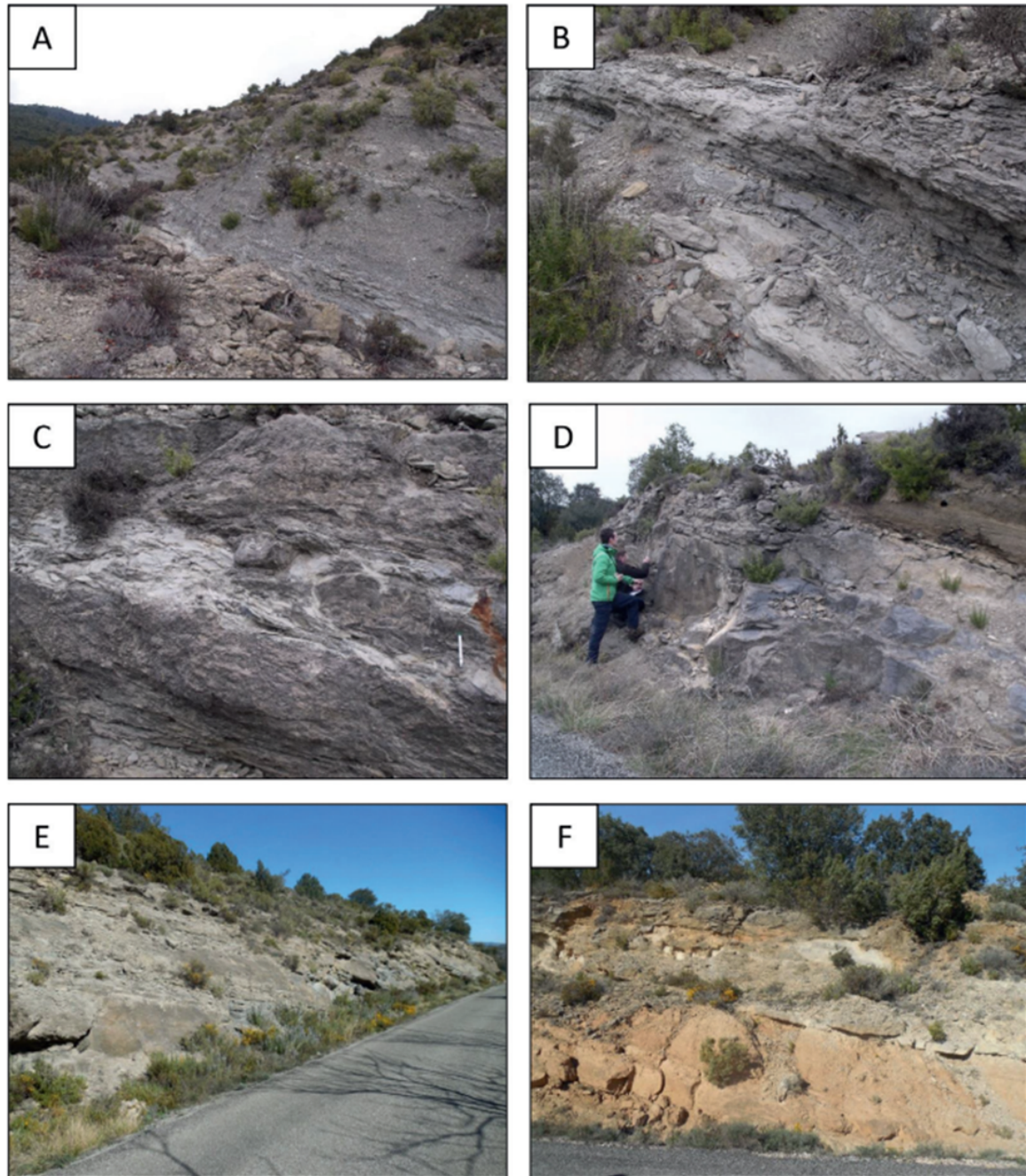
Figure 2.7: Outcrop images taken from the road of Arcusa-Mondot. A: Prodelta mudstone deposits. B: Distal delta front sandstone deposits. C: Delta front thick-bedded sandstone deposits. D: Proximal delta front cross-bedded sandstone deposits. E: Lower delta plain deposits. F: Fluvial channel conglomerate deposits interbedded with floodplain siltstones deposits [25]

3

Dataset

3.1. Area of Interest

In this study, a reservoir model inspired by the Sobrarbe Deltaic Complex outcrop is used to conduct CO_2 storage applications. The outcrop is located in Ainsa near Mondot, northeast of Spain. The outcrop illustrates clear delta lobes in the direction of the northwest. As illustrated in figure 3.1, the area of interest approximate dimensions are 1000 m in length and 1000 in width. The elevation of the outcrop approximately ranges from 665 m to 765 m and the elevation of the outcrop increases toward the direction of northwest. The outcrop consists of two hills separated by a road, the mountain pass road allowed for a lot of studies to be conducted.
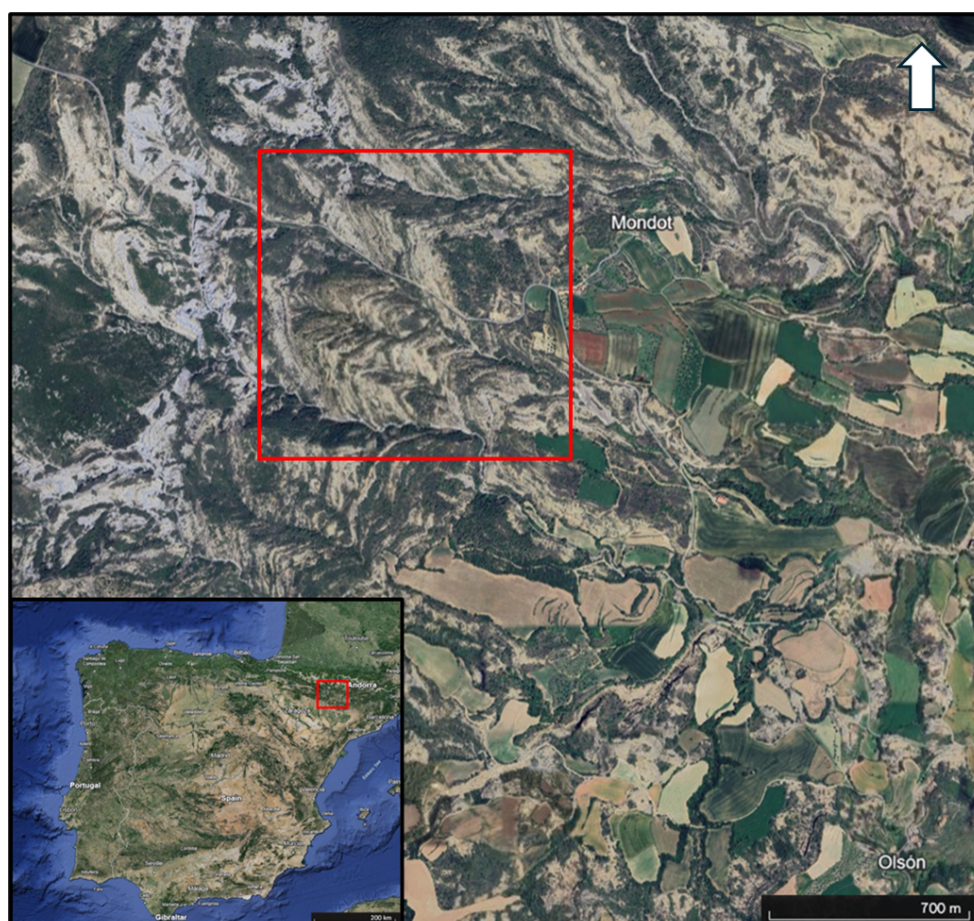
Figure 3.1: A Google satellite image of the area of interest near Ainsa, northeast of Spain. The red rectangle indicates the focus of the study [26]

3.2. Geological Data

The main used data in this study are core data, petrophysical data, and sedimentary log sections.

3.2.1. Core Data:

The available core was extracted from the Mondot-1 well after it was drilled in the year 2014 southwest of Mondot village, the location of the well is illustrated in figure 3.2. The total depth of the well is 185 m with a starting depth of 0 m. The core diameter of 10.5 cm and using the wireline logs, the depth was corrected with a shift of 0.75 m. Almost 95% of the core was extracted indicating a very high recovery percentage with an inclination of 9 degrees. Core plugs were extracted from the core for further analysis such as porosity and permeability measurements. Within the core, 196 plugs were used to measure porosity, and 50 plugs were used for permeability, the permeability points are overlaying the porosity points as illustrated in figure 3.4. For spacing between plug points, no increment was used as the spacing between plugs differs. Then the core was slabbed for core description. The core is stored in Nederlandse Aardolie Maatschappij store in the Netherlands [20].
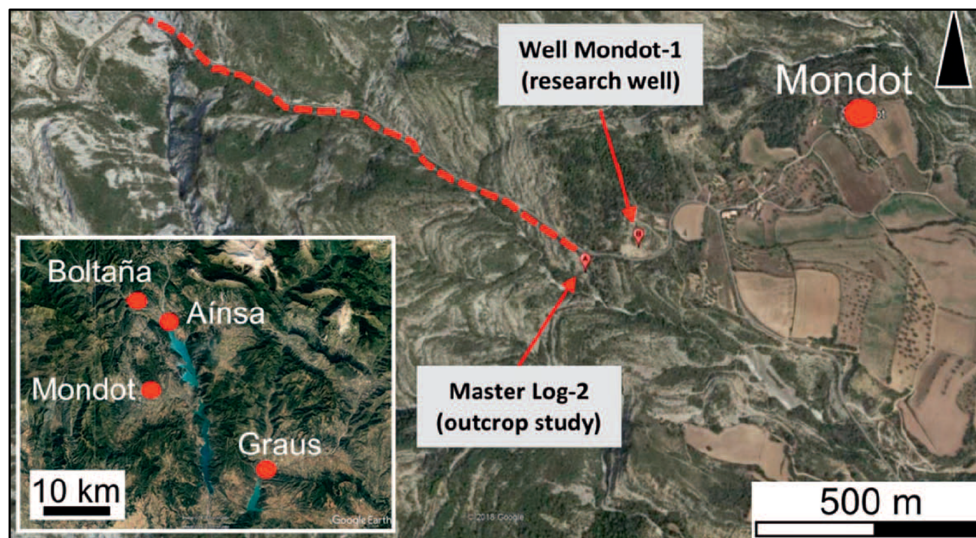
Figure 3.2: A location map indicates the location of Mondot village, Mondot-1 well, and the path of the sedimentary log section. In addition, the location of main cities or villages are indicated in the figure [12]

The core covers depositional environments within the Sobrarbe Deltaic Complex from alluvial to prodelta environments. The base of the distal delta front is marked by marly claystone deposits representing the prodelta environment at a depth of 154 m. The boundary between the Comaron Composite Sequence and the Las Gorgas Composite Sequence is marked at a depth of 81 m and is considered the boundary between the delta front and the delta plain depositional environment within the Sobrarbe Deltaic Complex. The two depositional environments are distinguished by a significant decrease in bioturbation (from the delta front to the delta plain). The top of the upper delta plain is marked by conglomeratic sandstone deposits with an increase in the level of bioturbation representing the beginning of alluvial deposits at a depth of 30 m In addition, several silty layers are identified that can be a barrier if it's continuous and need to be further investigated. A 1 m thick silty layer is observed at a depth of 118 m within the distal delta deposits. Another silty layer is observed at a depth of 78 m with an approximate thickness of 2 m, as illustrated in figure 3.4 [20].

3.2.2. Petrophysical Data: Porosity and Permeability

Porosity and permeability data are the main factors in this study and will be used to evaluate the heterogeneity of the reservoir inspired by the Sobrarbe Deltaic Complex outcrop and the effect on CO_2 injection and storage applications. Porosity and permeability values are retrieved from two main sources. First, using plugs that were extracted from the Mondot-1 core. The plug points for both porosity and permeability

are illustrated in figure 3.4 and retrieved from [20]. The second source is literature, four sources were used to retrieve porosity and permeability data assigned to the mentioned facies associations considered in this study. All the data in the sources are retrieved from core data from wells. The depth of the wells ranges from 2500 to 3500 m and the criteria of choosing data was based on the similarity of facies association and facies between the sources and this study, table 3.2 illustrated the gathered porosity data represented by average porosity for each facies association.

Table 3.1 summarizes the reading of plugs measurements for porosity and permeability. The analysis is done by calculating average and max values for each facies association. For porosity, the maximum value for the entire facies association is 18%, the minimum is 1% and the average porosity is 9%. For the permeability values, the range is between 0.03 mD to 10 mD. In general, the values for both porosity and permeability are extremely low and it will not reflect reservoir characteristics for the simulation phase.

Depth [m]	Facies Association	Avg Porosity [%]	Max Porosity [%]	Avg Permeability [mD]	Max Permeability [mD]
157 - 165	Prodelta	1	2	-	-
157 - 117	Distal delta front/prodelta	4.4	7.5	2	10
117 - 118	Distal delta front/prodelta	-	-	-	-
118 - 95	Distal delta front	4	8	0.5	1
95 - 90	Proximal delta front	4	8	0.03	0.03
90 - 81	Proximal delta front	5.5	14	3.5	10
81 - 78	Lower delta plain	3.5	10	0.5	1
78 - 76	Lower delta plain	-	-	-	-
76 - 60	Lower delta plain	3.5	10	0.5	1
60 - 50	Upper delta plain	3	7	0.7	1
50 - 30	Upper delta plain	5	10	2	10
30 - 0	Upper delta plain/mouth bar	9	18	2	10

Table 3.1: The facies associations retrieved from the core are linked to depth, arithmetic average porosity, and max porosity. Arithmetic average permeability and max permeability, data are analyzed using plugs from Mondot-1 core [20]

Facies Association	Average Porosity [%]	Average Permeability [mD]	Source
Delta Front	22	400	[27], [28]
Upper Delta Plain	27	1013	[28], [29]
Lower Delta Plain	27	560	[28], [29]
Mouth Bar	29	2350	[27], [30]
Channel Belt	29	3000	[27], [30]
Marly siltstone	0.5	0.4	[27], [30]
Prodelta	3.5	5.4	[30]

Table 3.2: Summary of gathered data represented by average porosity and permeability data from six literature sources, [27], [31], [30], [32], [29] and [28]

The well of Mondot-1 is provided with several log data, which were used to identify the lithology of the penetrated layers in the well as illustrated in figure 3.4. For lithology identifications, the main wireline logs that can be used are gamma-ray, sonic, density, and PeF logs. Tabel 3.3 summarize the log data for generalized facies and retrieved from [12].

Facies	GR [API]	Sonic [us/ft]	Density [g/cm^3]	Neutron [pu]	PeF [b/e]
Marly siltstone	60 - 100	-	2.4 - 2.6	15 - 25	3.8 - 4
Bioturbated silty sandstone	50 - 60	200	2.61 - 2.69	15	4
Bioturbated thick-bedded sandstone	40	160	2.66	5	4.1
Cross-bedded sandstone	35 - 45	170 - 180	2.65 - 2.68	5 - 10	4.1
Pebbly sandstone	25 - 40	160 - 170	2.64 - 2.7	4 - 10	4 - 4.5
Conglomeratic sandstone	30 - 60	160 - 170	2.6 - 2.7	4 - 15	4 - 4.5

Table 3.3: Generalized facies and their log data ranges, the log data are Gamma-ray, Sonic, Density, Neutron, and PeF logs. The data are retrieved from [20]

3.2.3. Sedimentary Log Sections:

The correlation between the sedimentary log section and core can enhance the understanding of the possible lateral extension of the facies within the Sobrabre Deltaic Complex outcrop. However, the correlation between cores and cross-sections must consider several factors such as lateral extension, compaction, elevation changes, and weathering that affect porosity and permeability. Figure 3.2 illustrates a sedimentary log section, which is an outcrop study presented by Marshall el al. [20]. On the Arcusa-Mondot road, the sedimentary log section covers approximately 1.3 km of the road, which represents a thickness of almost 300 m. The sedimentary log section presented by Marshall et al [20]. shows that the delta plain and delta front are well-correlated with the core in terms of facies and thickness. The sedimentary log section shows a similar trend of bioturbation, specifically at the boundary between the Las Gorgas composite sequence and the Comaron composite sequence with the core data. However, the alluvial and prodelta environments are not correlatable with the core and show significant variations in thicknesses. Two major silty layers, which can be a barrier in reservoir simulation indicated in the core data section are detectable in the log section as illustrated by red rectangles in figure 3.3. A 1 m thick silty layer is observed at a depth of 118 m within the distal delta environment. Another silty layer is observed at a depth of 78 m with an approximate thickness of 2 m. The focus on these two layers as they represent the thickest silty layers and have a clear correlation between the core and the sedimentary log section.
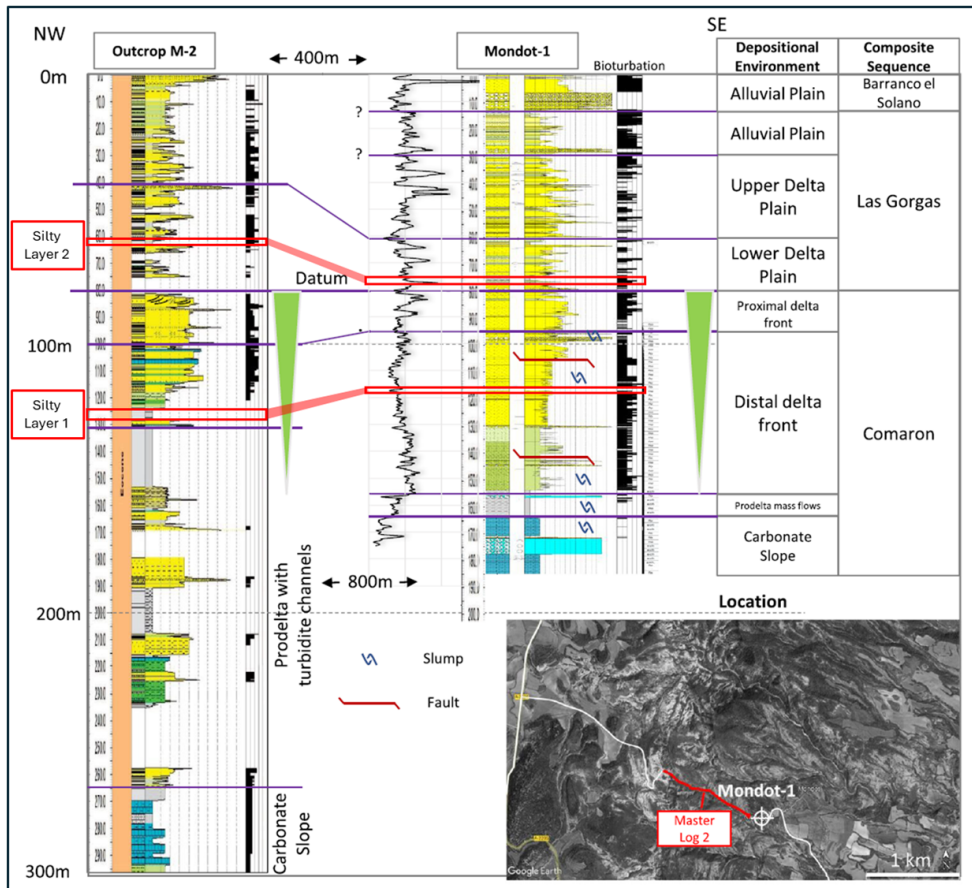
Figure 3.3: A correlation between sedimentary log section "Master Log 2" and Mondot-1 well with indicating the depositional environment and composite sequences within the covered depths or elevations, red rectangles indicates two silty layers [20]
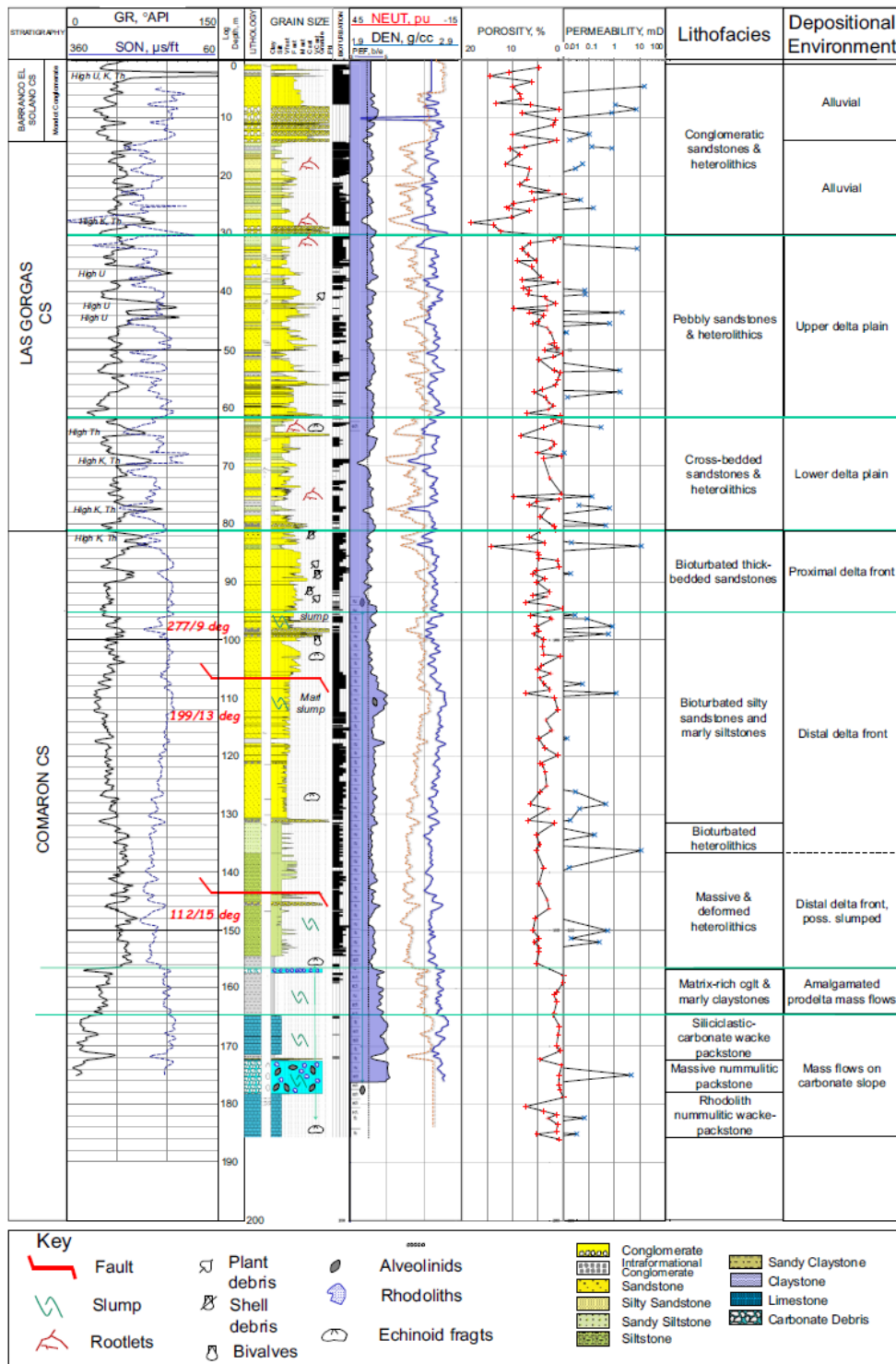
Figure 3.4: Composite log of Mondot-1 indicating core descriptions and plug data as geological data and logs as petrophysical data include: Gamma-ray, sonic, neutron, density, and photoelectric absorption log [20]

<div align="right">

4

</div>

Methodology

4.1. Analyzing Satellite Images

Google Earth was used to provide high-resolution satellite images of Earth's surface that can be used to capture geological features that correlate with previous data types. As illustrated in figure 3.1, the satellite image from Google Earth indicates the Sobrarbe Deltaic Complex outcrop, approximately 1 km by 1 km. In addition, the street view tool, which is a tool that allows one to navigate through 360-degree images of streets around the world and is captured by Google's street view vehicles. The tool provides clear images of the outcrop through the Arcusa-Mondot road as illustrated in figure 4.1. The Arcusa-Mondot road is cutting through the outcrop providing clear images of the geological features within the Sobrarbe Deltaic Complex. Google Earth provides elevation points for the outcrop that will be used in the next sections to compare the calculated thickness of deposits from Google Earth with the Mondot-1 core.

Figure 4.1: Google Satelite image, the blue line between the two hills illustrates the roads with street view availability [26]
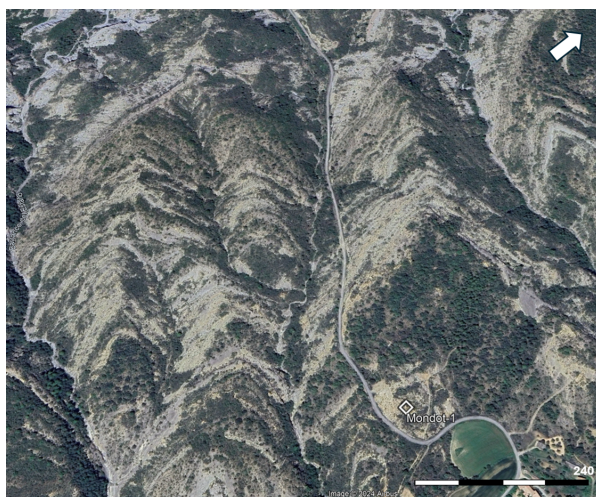
Figure 4.2: A satellite image retrieved from Google Earth for area of interest with a location of Mondot-1 Well, [26]

The first approach to reaching the framework cross-section was marking the recognizable surfaces on the satellite image. The main factor in drawing the lines is clear color changes that can be traced along the area of interest. For quality check, the marked surfaces are investigated using the tool "street view" at the point that crosses the Arcusa-Mondot road as illustrated in figure 4.1. The "street view" tool allows for investigating the marked surface by outcrop images as illustrated in figure 4.3. In addition, the surface line between two composite sequences (Comaron Composite Sequence and Las Gorgas Composite Sequence) was already provided and considered a reference line as it separates two facies associations [33].

Figure 4.3: An image from "street view" in Google Earth indicates the location of marked surfaces, the red line marks the surfaces where an expected change in color, the location of the image is line 3 in figure 5.3, [26]

The regional dip was corrected in the area of interest to measure the true vertical thicknesses between drawn surfaces. The first step is calculating the distance between the marked surfaces from the map view aspect. Several distances were measured in each layer and the average was considered. Then, by applying Pythagoras theorem with an angle of 17.5 degrees, the true vertical thickness can be estimated. The measured true vertical thickness between surfaces is aligned with the Mondot-1 core facies associations scheme to link the potential traced lateral variability of facies from the satellite image with the facies associations classification based on Mondot-1 core. The report captures the facies association scheme that was interpreted from the Mondot-1 core, which represents a decameter heterogeneity scale.

4.2. Process of Building the Base Model

For this project, the static models will be built using Rapid Reservoir Modeling (RRM). The software allows for building and modifying rapid and complex geological 3D models. The rapid building provides the ability to investigate the uncertainties of the reservoir model by testing different scenarios. The software is an open-source system developed by different partners [34]. RRM software uses Sketch-Based Interface Modeling (SBIM) technology and tools used to analyze reservoir behavior such as flow diagnostic. The 3D model can be built by two 2D approaches: the cross-sectional approach or the map view approach [35]. In this project, the map view was the base for sketching as the reference was an interpreted satellite image.

In the cross-sectional view, the Sketch Region (SR) tool was used to separate layers representing lateral changes and drawing channels. The four tools (RA, RB, RAI, and RBI) were used to create the surfaces that bound the layers. The four tools are briefly explained as the following: 1) RA: remove above, 2) RB: remove below, 3) RAI: remove above intersection, and 4) RBI: remove below the intersection. Remove above or below will lead to removing the crossing surface and all other surfaces above and below. While remove above instructions and remove below intersection will lead to only removing the crossing surface[35]. The cross-section view can be displayed in different orientations, north-south and west-east. The different orientations can provide better insight into the complex geological model in terms of layers and channels. Using RRM software, the proposed five facies associations in the Facies Associations of Sobrarbe Deltaic Complex section were sketched using the map view of the interpreted satellite image as a base and the vertical aspect from the core. In addition, both channel belt and mouth bar facies association dimensions including length and width are sketched by using literature data. Where the distribution and frequency of channel belts and mouth bars are concentrated in the upper delta plain and decrease until mouth bars and channel belts are terminated near the transition zone between the upper delta plain and lower delta plain. However, the number of mouth bars and channel belts used in the model is hypothetical.
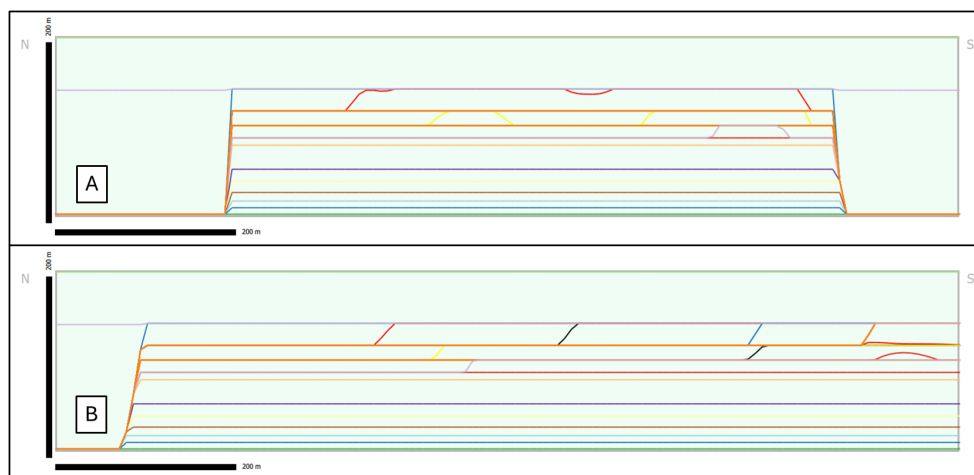
Figure 4.4: Cross-sections illustration, West-East (W-E) display in figure A and North-South (N-S) display in figure B from RRM software. The colors of the surfaces are arbitrary

4.3. Process of Building Different Realizations of the Reservoir

4.3.1. Petrophysical Properties:

The petrophysical properties considered in this study are porosity and permeability. The value of the petrophysical data from the Mondot-1 well is significantly low due to the full cementation of the core, figure 4.5 illustrates a thin section with almost no observable porosity. These low values will not properly reflect reservoir properties targeted in this project that acquire CO_2 injection with sufficient rate of injections, especially in a short time-scale simulation phase. For that, porosity and permeability data used in this study are retrieved from four literature studies and the plug data is ignored. The porosity and permeability data in the literature are retrieved from core plugs data in reservoir depths ranging from 2500m to 3500m. The link between the literature and this project was the similarity of facies associations and facies in

terms of lithology that was used in this study, table 3.2 summarized the gathered data. Two scenarios were built based on petrophysical aspects, high scenario associated with higher porosity and permeability data, and low scenario associated with lower porosity and permeability data. The two scenarios are calculated by the following, arithmetic average porosity and permeability of all facies associations were multiplied by a fraction of 10% for porosity and 20% for permeability, in permeability the fraction was higher as the arithmetic average values are relatively higher compared to the porosity and higher fraction in permeability will enhance the variations between low and high scenarios. The fractions for each arithmetic average porosity/permeability facies association were added for the high scenarios, and the fractions were subtracted for the low scenarios.

In this study, the x, y, and z directions for permeability are considered. X and y directions are equal. Generally, deltaic lobes are bound by changes in petrophysical properties that commonly affect vertical properties more than lateral properties, making vertical permeability lower than lateral permeability in reservoirs [36]. In this study, a factor of 10 is considered between vertical and horizontal permeability, the factor is not based on a geological approach but it was used to emphasize the differences between vertical and horizontal permeability. The summary of porosity and permeability data is provided in table 4.1

Figure 4.5: A thin section from Mondot-1 core illustrates delta plain facies association. The thin section shows well-sotred fine-grained sandstone with siltstone clasts, depth: 79 m [25]

4.3.2. Sketching the Silty Layers:

The continuous silty layers are sketched in RRM, by sketching two surfaces to mark the boundaries of the layer of silt within the other layers of deltaic deposits. The patchy scenario is based on the continuous silty layer and then modified by the sketched region "SR" tool to draw a zigzag line to emphasize the discontinuity of the defined layer. The zigzag line is sketched in one of the N-S cross-sections, and the software will propagate the sketched zigzag surface to the other lines.

Facies Association	High Scenario				Low Scenario			
	Poros-ity [%]	Permeability [mD]			Poros-ity [%]	Permeability [mD]		
		x	y	z		x	y	z
Prodelta	4	10	10	0.1	3	0.7	0.7	0.07
Delta Front	24	520	520	52	19	270	270	27
Lower Delta Plain	30	850	850	85	24	270	270	27
Upper Delta Plain	30	1125	1125	113	24	800	800	80
Channel Belt	32	3000	3000	300	26	2000	2000	200
Mouth Bars	32	2500	2500	250	26	1500	1500	150
Siltstone	1	0.8	0.8	0.08	0.2	0.003	0.003	0.0003

Table 4.1: Summary of porosity and permeability data with high and low scenarios that will be used in this study, gathered from literature sources: [27], [31], [30], [32], [29] and [28]
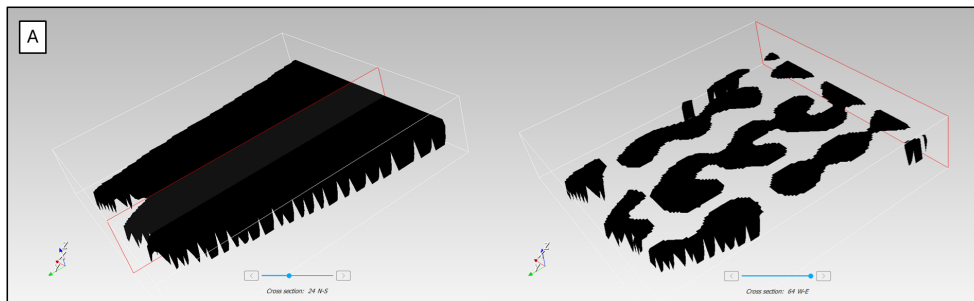
Figure 4.6: A 3D display for the silty layer with two different realizations, figure A shows a continuous layer and figure B shows a patchy layer

4.4. Process of Simulating the Static Models

The simulation phase in this project is conducted using the Computer Modelling Group Ltd "CMG". The software provides different modules that can be used in several applications including Carbon capture underground storage modeling. In this project, four main modules are used: CMG Launcher, Builder, Generalized Equation-of-State Modeling "GEM", and Results. In CMG Launcher, the grid files of the static models are uploaded and linked to an applicable template created for similar applications in this study. GEM Launcher is a compositional simulator designed for modeling gas injection processes such as CO_2 storage. It simulates the phase behavior of fluid components in the reservoir considering complex thermodynamic interactions and chemical reactions. Then, all parameters and rock properties are added in the Builder. In Builder, six models are available to supply the reservoir with all the needed details. The models are I/O Control, Reservoir, Components, Rock-Fluid, Initial Condition, and Wells and Recurrent. In the Reservoir, the grid is uploaded and the rock properties data is provided. The components model is based on the Model Equation of State "EOS" Peng-Robinson that uses composition data and generates densities and equilibrium phase compositions as a fluid model. In Rock-Fluid, Stone's Second Model "SWSG" is used to assess the rock fluid and to formulate relative permeability and hysteresis parameters. In the Initial Condition, the reference pressure and depth are assigned, and in Wells and Recurrent the injected well is created with all needed parameters Finally, the Results module is used to display the results by different plots and 3D models [37].

4.4.1. Dynamic Parameters:

During the simulation phase, the targeted subsurface reservoir is assumed to be a water aquifer. The aquifer inspired by the Sobrarbe Deltaic Complex outcrop is assumed to have a reference depth of 2000

m to ensure reservoir behavior where communally CO_2 is injected to be above supercritical CO_2 condition. With applying a gradient pressure of 0.1 Pa/m on the reservoir, a reference pressure of 20000 kPa is considered [38]. The density of CO_2 is calculated depending on the depth and temperature of 50 degrees to be 780 kg/m^3 [39]. The lithostatic pressure of the reservoir is calculated by multiplying reservoir depth by gravity by average sandstone density (2500 kg/m^3 [40]) to be 53000 kPa. From the lithostatic pressure, the operational reservoir pressure limit is calculated to be 37000 kPa by using the rule of 70% limit, which was used to ensure that the pressure in the reservoir will not exceed 70% of the fracture pressure. The water density is 998 kg/m^3. The rock compressibility is 5.8e-7 1/kPa. The relative permeability for this project is extracted from the CMG library, due to the lack of experimental data for the Sobrarbe Deltaic Complex. In addition, the simulation is applied with closed boundary conditions. For the hysteresis modeling, the LAND model was used with a maximum residual gas saturation of 0.425 as the default value in CMG. The LAND model simulates the residual trapping of CO_2 during the imbibition process in a drainage-imbibition cycle. It accounts for the process of the non-wetting phase displacing the wetting phase and its reverse process [41].

4.4.2. Simulation Runs:

In this project, 4 runs will be conducted. The four runs are applied using an injection rate of 400 m^3/day at reservoir conditions. The simulations will be conducted for 100 years, the first 50 years is the injection phase and then the reservoir will be monitored for another 50 years without injection. In this project, only one injection well is used for the simulation. The runs are summarized in table 4.2

Model	Injection Rate (m^3/day)
Base Model	400
Model 2	400
Model 3	400
Model 4	400

Table 4.2: Summary of simulation runs for this project

4.5. Assessing the Simulated Models

The results of simulating the static models will investigated in this study to analyze the influence of reservoir heterogeneity of the Sobrarbe Deltaic Complex reservoir on the injection of CO_2 for a defined time scale. The analysis will cover three main points: the CO_2 plume migration, the injection rates, and the total mass of CO_2. In addition, the differences between the four scenarios will be part of the analysis to capture the most effective factors.

<div style="text-align: right; font-size: 3em;">5</div>

Geological Data Analysis

5.1. Satellite Image

Figure 5.1 illustrates the Sobrabre Deltaic Complex "AOI" retrieved from Google Earth with the dimension of 1 km by 1 km. The interpreted surfaces are illustrated in figure 5.1, with 7 surfaces representing the potential lateral continuity of facies distribution within the Sobrarbe Deltaic Complex. Surface line 4 is a reference line representing the boundary between two composite sequences and two different facies associations: Proximal delta front to Lower Delta Plain [33]. surface 1 marks the base of the Distal Delta front and the top of the prodelta mass flows, figure A in 5.4 illustrates the location of surface 1. Surface 7 marks the top boundary of the Sobrarbe Deltaic Complex represented by the transition zone between the fluvial and deltaic deposits.

Then, based on the thickness perspective the surfaces are correlated with the facies association classifications retrieved from the Mondot-1 core in figure 3.4. The total vertical thickness calculated for each layer bounded by surfaces is used as a guide and quality check process to populate the surfaces with the Mondot-1 core facies association scheme. Figure 5.2, illustrates the elevation points and distances between all surfaces. From these distances and elevation points, the true vertical thicknesses were estimated, illustrated in table 5.1. Comparing the estimated true vertical thicknesses with thicknesses from the core, the total estimated thickness from the satellite map is approximately 102 m, while the total thicknesses from the core for considered facies associations is 106 m. In general, the thicknesses of the bounded surfaces compared with the thicknesses of facies associations in the core show variations of 2% to 7%. However, the vertical distributions of the facies retrieved from Mondot-1 core were used in this study.

The "street view" tool images are illustrated in figure 5.4 and locations are indicated in figure 5.1. Images from the "street view" were taken at the intersection of the 7 surfaces with the road of Arcusa-Mondot road. The images were used for quality control purposes where lithology was interpreted based on color changes and structural features observed in the "street view" images. However, these interpretations come with high uncertainty as it's only based on medium to high-resolution images. The observations are as the following: Figure A 5.4 was taken from between the intersection of surface 1 with the road. The image shows dark layer deposits that could indicate dark shale deposits within the prodelta and delta front transition zone. Figures B and C 5.4 taken at Surface 2 and 3 along the road show a significant color change from dark gray to yellowish, which could indicate sand deposits within the delta front. The only possible cross-bedding feature observed using the "street view" at line 5 along the road is illustrated in Figure D 5.4.

Figure 5.3 illustrates the lateral distributions using the satellite image with the vertical distributions from the Mondot-1 core. The results come with high uncertainty as the link is between low resolution (Google Earth) and high resolution (Mondot-1 core). However, the thicknesses comparison between both source and image observations are used to mitigate the uncertainty as much as possible.
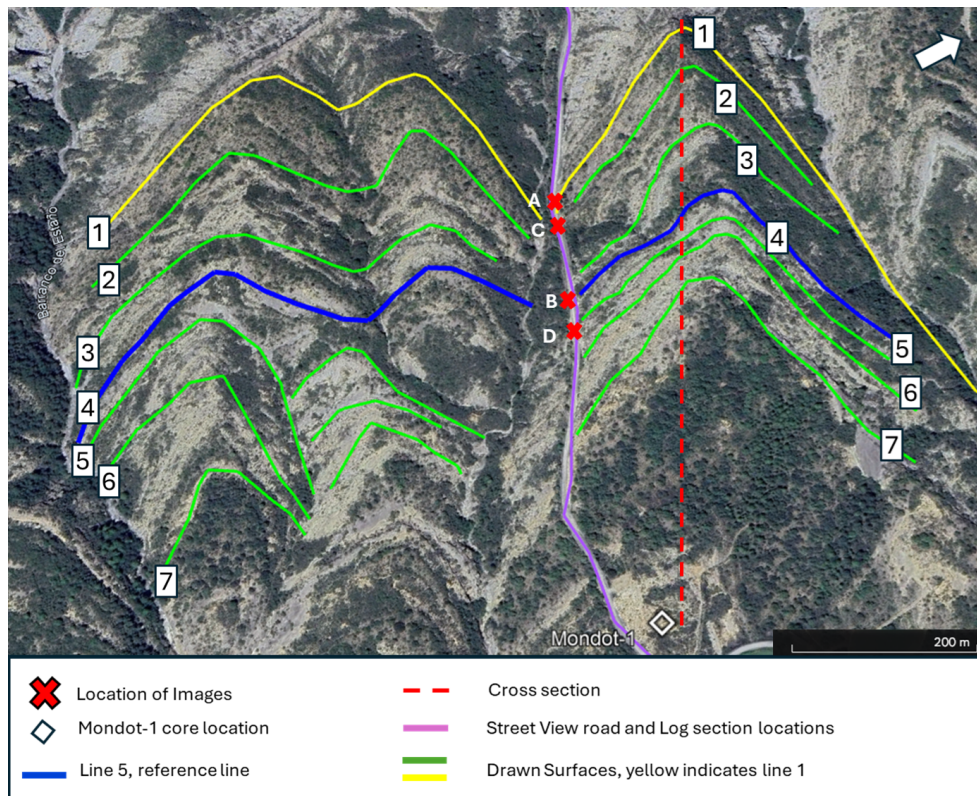
Figure 5.1: A satellite map retrieved from Google Earth for AOI with a location of Mondot-1 Well and with sketched lines numbered from 1 to 7, the red crosses indicate the location of images taken from "street view" and location of Mondot-1 core is displayed in the map
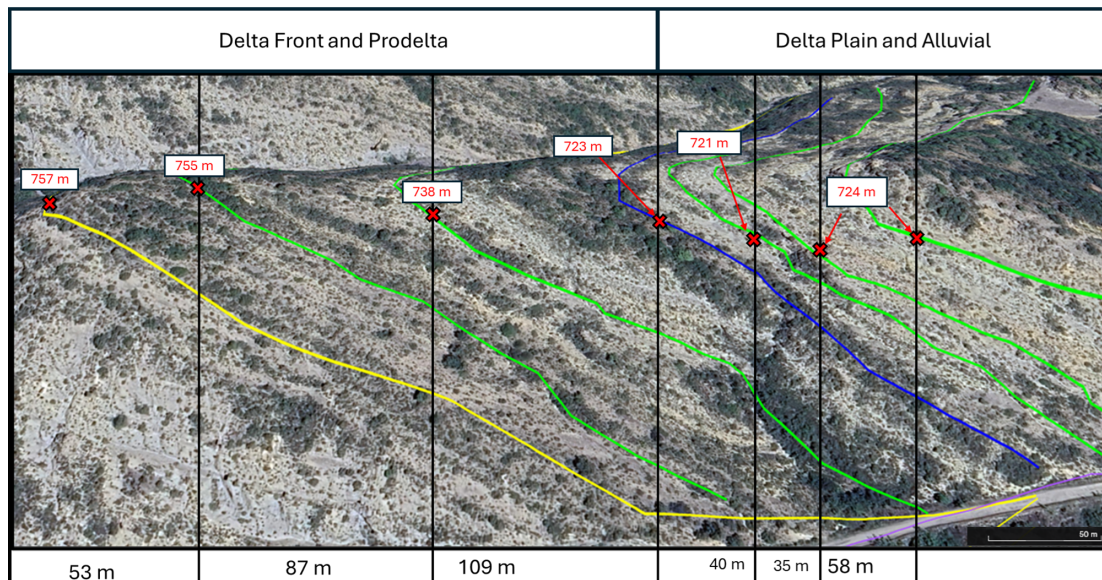
Figure 5.2: An image of the outcrop from Google Earth overlayed by surface lines and elevation points

Bounded Surfaces	Distance [m]	True Vertical Thickness [m]	Thickness From The Core [m]
1-2	53	16	18
2-3	87	26	26
3-4	109	33	34
4-5	40	12	13
5-6	35	11	12
6-7	58	17	20

Table 5.1: Measured vertical thicknesses from the satellite image are compared with thickness from Mondot-1 core within the bounded surfaces
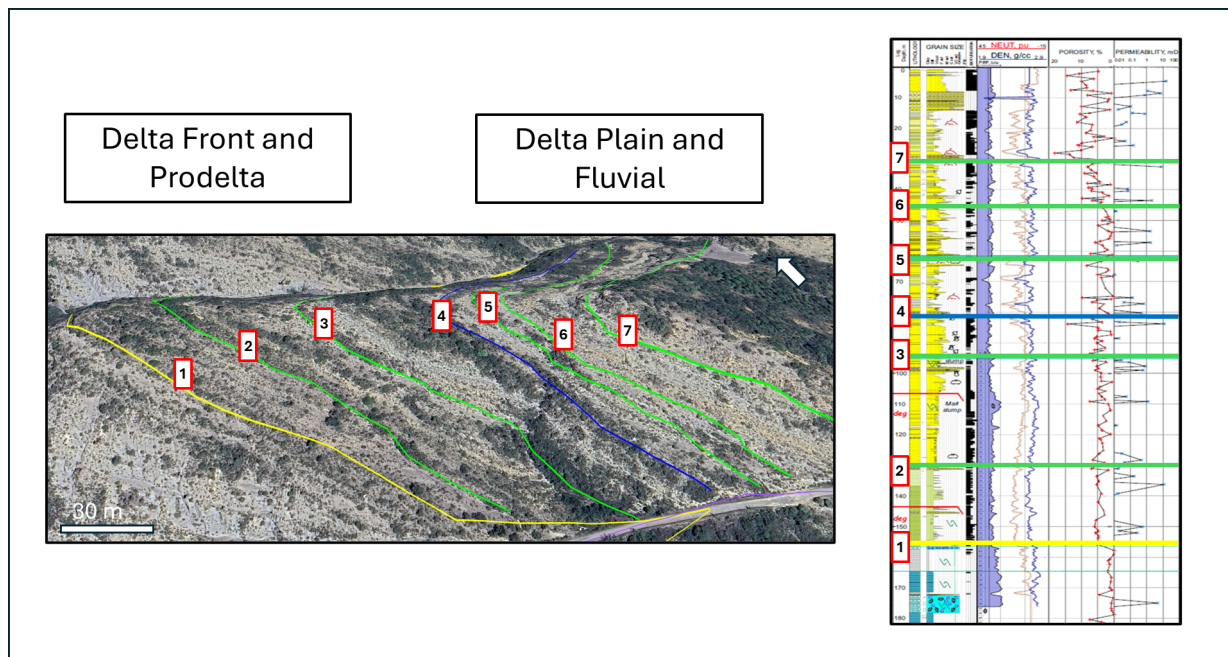
Figure 5.3: The Mondot-1 core correlated with the satellite image surfaces numbers
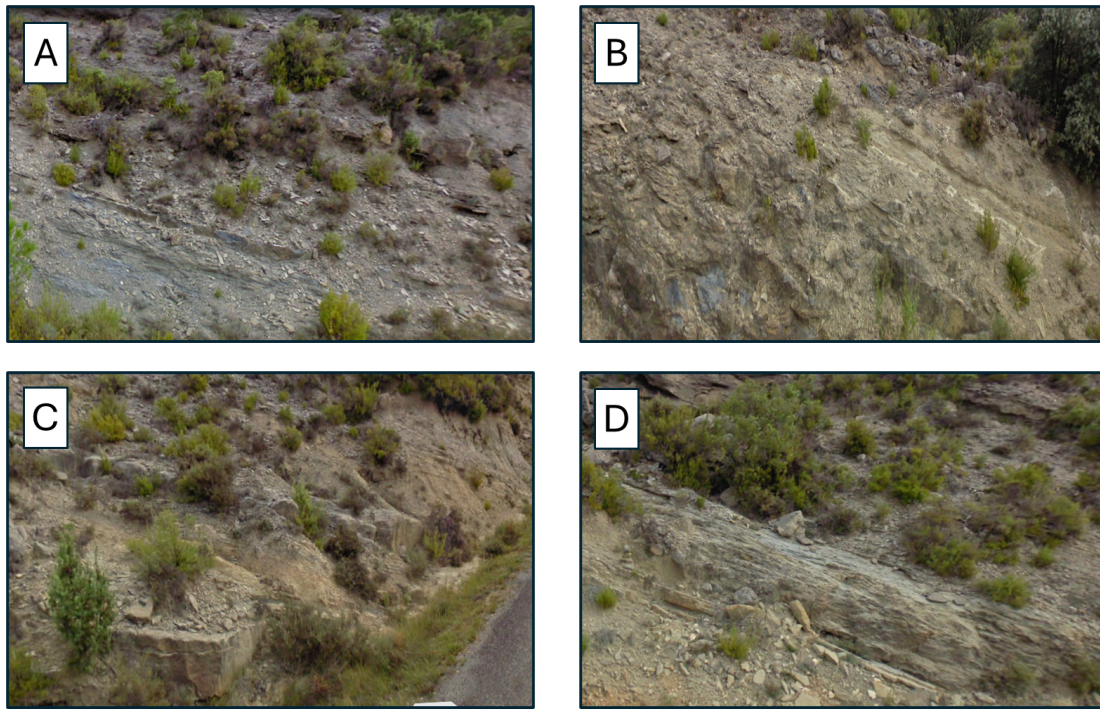
Figure 5.4: 5 images retrieved from Google Earth Engine, using "street view" tool, A: indicate the location of surface 1, showing siltstone deposits on top of dark shale deposits, B: indicate a location between surface 2 and surface 3 with deposits of siltstone, C: an image from location 3, representing the first sand deposits, D: an image at surface 4, illustrating bedded sandstone deposits and E: an image at surface 6 indicates a cross-bedding feature in sandstone deposits

5.2. Cross Section

The cross-section for the reservoir inspired by the Sobrarbe Deltaic Complex outcrop in this study was built by capturing the potential lateral distribution of facies associations deposits from marked surfaces in Google Earth images and the vertical distribution of facies associations deposits from the Mondot-1 core. The result is illustrated in figure 5.5. The schematic cross-section captures two layers of silty facies observed in the core and sedimentary log sections. In the Mondot-1 core, several silty layers can be observed. However, the two layers are chosen as they represent the thicknesses, ranging between 1 to 2 m that can be captured in the reservoir model. The depths of the silty layers are 118 m and 87 m in Modnot-1 core, figure 3.4.From base to top of the cross-section, the delta front is considered the bulk of the outcrop cross-section followed by the Lower delta plain. In the Upper delta plain, the transition between the deltaic and fluvial environment is captured by deposits of mouth bars and channels. The influx of fluvial deposits extends to the Upper Delta Plain. The shallowest deposits are the channel belts with a background of mudstone sheets. The cross-section is inspired by the Sobrarbe Deltaic Complex outcrop. However, the primary goal of this study is to replicate the outcrop cross-section to reflect the condition of a reservoir, allowing CO_2 storage analysis. For that, figure 5.6 illustrates the same cross-section but in reservoir condition. The main criteria to reflect the reservoir inspired by the Sobrabre Deltaic Complex outcrop is adding the eroded deposits by weathering in the reservoir cross-section. Walther's law is applied as observed facies association in the vertical aspect can be reflected in the lateral aspect [42]. Where vertical distribution of facies associations in the outcrop cross-section is applied laterally in the figure 5.6 to encounter the eroded parts in the outcrop.
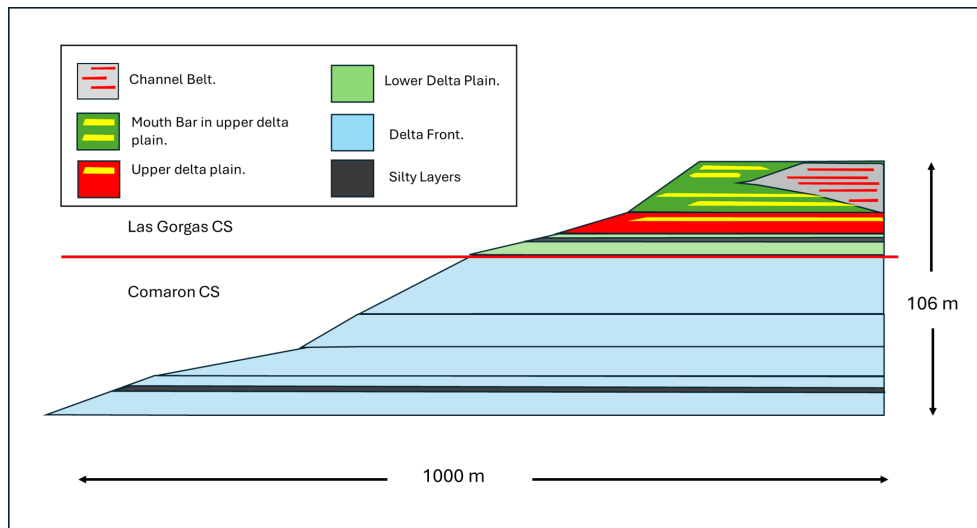
Figure 5.5: A schematic cross-section of the vertical and lateral distribution of facies associations of Sobrarbe Deltaic Complex Outcrop based on the interpretations of the satellite map and Mondot-1 core, the location of the cross-section is indicated in figure 5.1
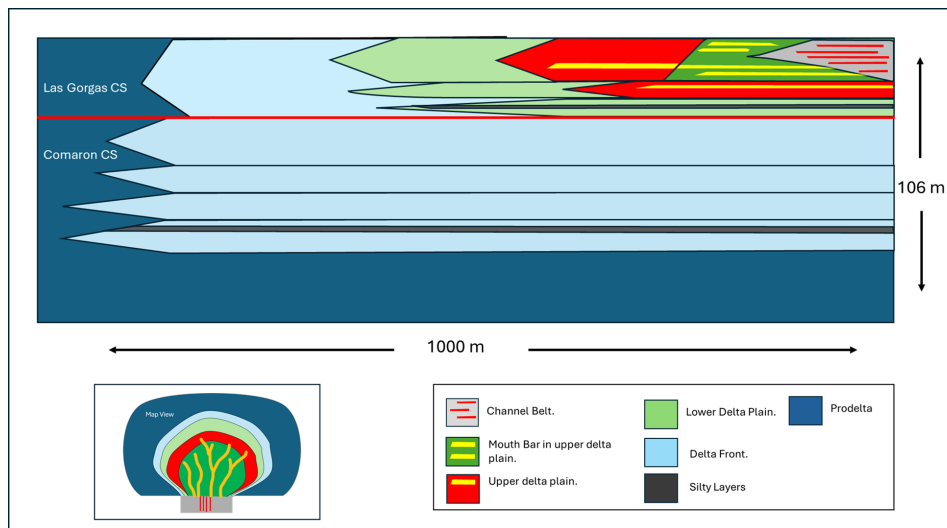
Figure 5.6: A schematic cross-section of the vertical and lateral distribution of facies associations of a reservoir inspired by Sobrarbe Deltaic Complex Outcrop based on the interpretations of the satellite map and Mondot-1 core including the eroded part to mimic reservoir analog, a map view of the cross-section is included, the location of the cross-section is indicated in figure 5.1

6

Static Model

All realizations of static models are generated using RRM software. The first phase was building the outcrop model as the reference of this study is based on satellite images 5.1. Then, the analog model mimicking a reservoir model was built. The first analog model is the base model, representing the petrophysical properties of the log and core data and the continuous silty layers mentioned in the literature and defined in the core data and log sections. Then, different realizations will be introduced, Model 2, Model 3, and Model 4.

6.1. Outcrop Model

Figure 5.5 illustrates the reference model, which represents the outcrop analysis. The model with a dimension of 1 km by 1 km is not used in the simulation phase but it is used as a reference for building the reservoir model. As illustrated in figure 6.1, the outcrop model follows the geometry of the satellite image interpretation and was built using RRM software. In addition, the color of the model is based on the legend found in figure 5.5 and 5.6.
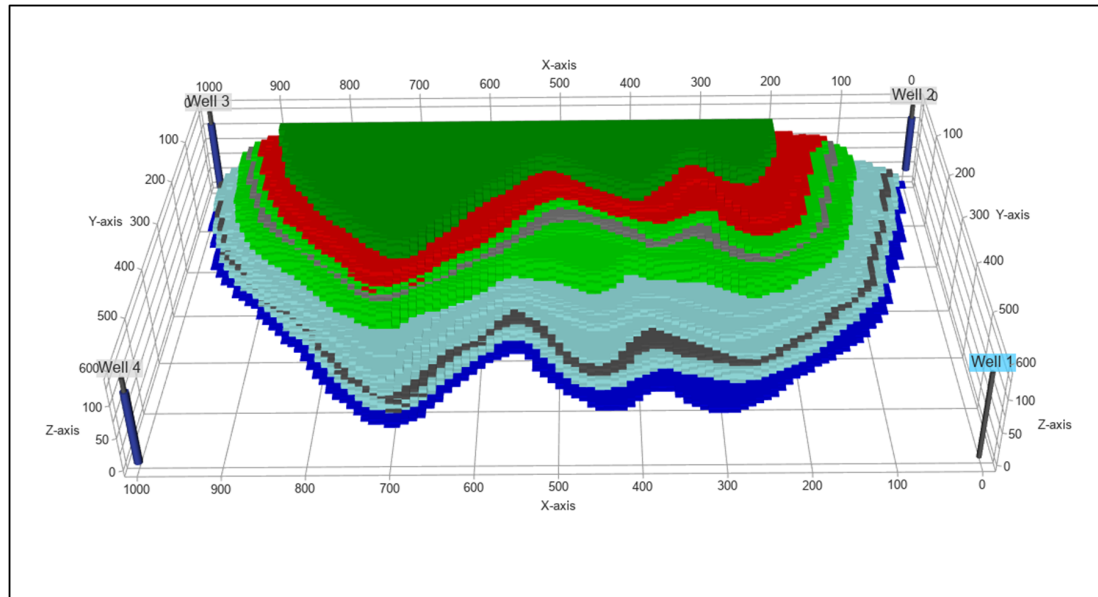
Figure 6.1: A model for the outcrop with a grid resolution of 21x21x21, with two silty layers. Legend of the colors: dark blue: Prodelta, light blue: Delta front, light green: Lower delta plain, red: upper delta plain, dark green: Mouth bar in Upper delta plain

6.2. Reservoir Models

The outcrop model and cross-section are adjusted to mimic the subsurface reservoir behavior. One of the main modifications is adding the eroding parts by applying Walther's Law laterally and vertically. The results of these modifications are illustrated in figure 6.2. Figure A in 6.2 indicates the map view of all layers, while the geometry is still preserved from the outcrop model. In Figure B, the first layer of the upper delta plain is removed to illustrate the channel "red" and mouth bars "yellow" deposits. The channel and mouth bar extensions are within the upper delta plain and the frequencies of the belt decrease laterally and vertically. In addition, the prodelta laterally surrounds the deltaic deposits, specifically the distal delta plain, and the prodelta is characterized by low porosity and low permeability and will be considered to be a lateral cap to the reservoir. The colors of the layers are based on the schematic cross-section legend in figure 5.6

In addition, 4 different realizations are considered in this study as illustrated in table6.1. The base model captures the two silty layers observed in logs and log sections, and the high scenario of the porosity and permeability, data are summarized in table 4.1. Model 2 considers patchy silty layers and high scenario porosity and permeability measurements. Model 3 considers continuous silty layers and low petrophysical scenario. Lastly, model 4 with patchy silty layers and a low scenario for the petrophysical measurements.

# of Models	Silty Layer	Petrophysical Scenario
Base Model	Continuous	High Scenario
Model 2	Patchy	High Scenario
Model 3	Continuous	Low Scenario
Model 4	Patchy	Low Scenario

Table 6.1: Summary for the 4 realizations considered in this study
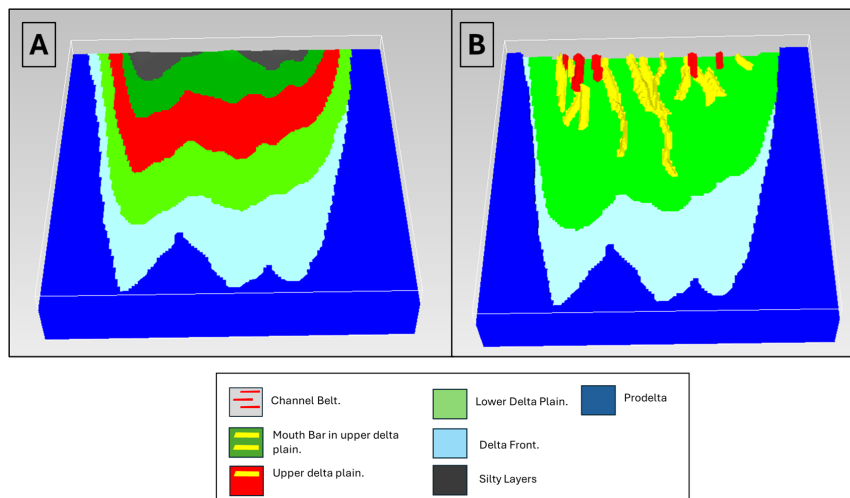
Figure 6.2: A reservoir model generated using RRM. A: the full depositions are included. B: Some layers are not displayed to emphasize the channel distributions

6.2.1. Base Model

The base model was created to capture the geometry of the outcrop retrieved by satellite images and to capture the geological variations laterally and vertically based on core data and literature. In addition, the thickness of the layers is defined by measuring the vertical thickness from the satellite images and modified using the regional dip angle to calculate the true vertical thickness, table 5.1. The dark blue facies association is the prodelta and it's captured here to cap the reservoir laterally.
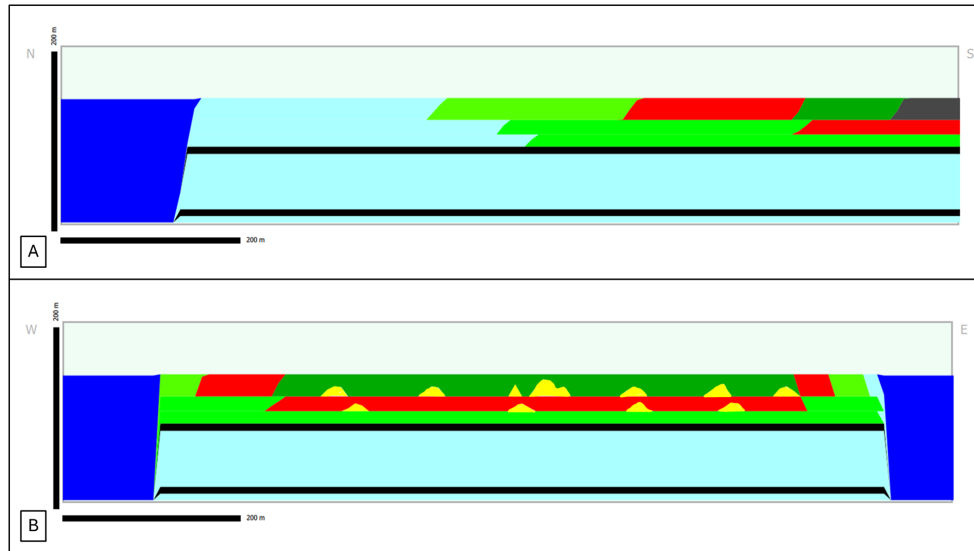
Figure 6.3: Cross-sectional display to the base model, A indicates the North-South cross-section and B indicates the West-East cross-section. The black layers are the silty layers

In addition, the porosity and permeability data are assigned using the high scenario measurements from table 4.1. The core and logs indicated several silty layers, two main silty layers were chosen to be in the base model as they represent a significant thickness and can be captured both in the core and log sections as illustrated in figure 6.3 and in the base model it will be assumed continuous.

6.2.2. Model 2

Model 2 shares the same petrophysical data as the base model but with patchy silty layers. Figure 6.4 illustrates the North-South cross-section and West-East cross-section that indicates the discontinuity of silty layers. In this model, both silty layers are patchy and drawn in a random approach to assess the effect of these layers. In figure 6.5, A represents the upper silty layer just below the upper delta plain, the surrounding of the silty layer is assumed to be the deposits of the delta front.
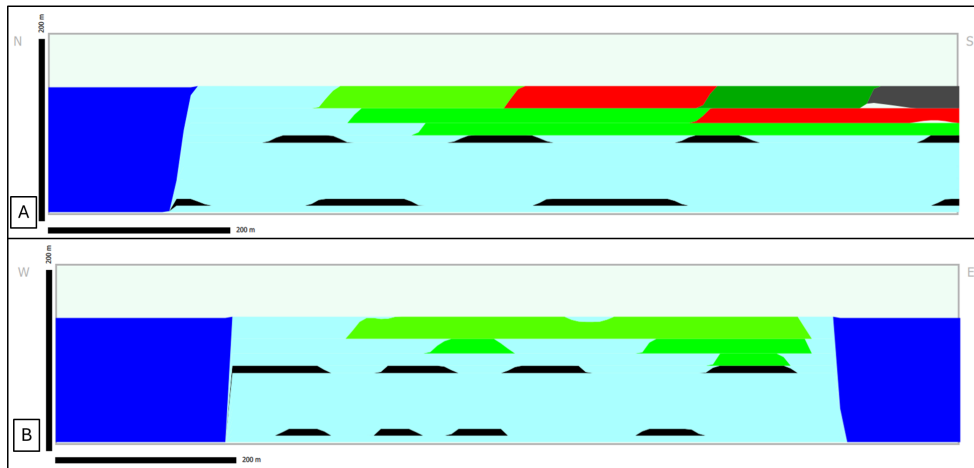
Figure 6.4: Cross-sectional display to model 1, A indicates the North-South cross-section and B indicates the West-East cross-section. The black layers are the silty layers. Cross-section: 55 W-E

The variations in the geometry of the two silty layers are implemented to assess the effect of the geometry and continuity of these layers. B in figure 6.5, indicates the lower layer and shows smaller patches of silts, which lead to less continuity. As the porosity and permeability data are the same as the base model, model 2 is heavily influenced by the silty layers and will assess the flow with less barriers relative to the base model.
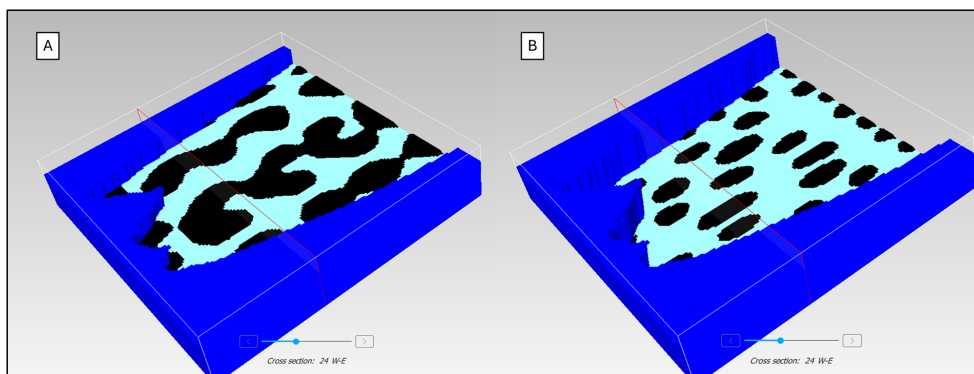
Figure 6.5: 3D display for the silty layers in Model 1, A displays the upper silty layer and B displays the lower silty layer

6.2.3. Model 3

Model 3 captures the continuous silty layers, similar to the base model as illustrated in figure 6.3 but using low scenario for the porosity and permeability, table 4.1.

6.2.4. Model 4

Mode 4 is linked to a low scenario for porosity and permeability, 5.1 and with patchy silty layers similar to model 2 as illustrated in figure 6.4 and figure 6.5.

6.3. Grid Resolution

The reservoir models in this project are complex and contain sufficient layers and geological features that need proper grid resolution to be fully captured and ready for the simulation phase. However, with higher resolution grids, higher processing time in the simulation phase. As the period of this project is limited, the balance between sufficient grid resolution that captures the geological features and simulation time

needs to be balanced. One of the major points in deciding the proper grid resolution is the continuity of the channels, the distribution of the channels is illustrated in figure B 6.2. The default grid resolution in RRM software is 21 x 21 x 21 as displayed in figure 6.6, with this resolution the channels are barely captured. For that, a higher resolution is needed.
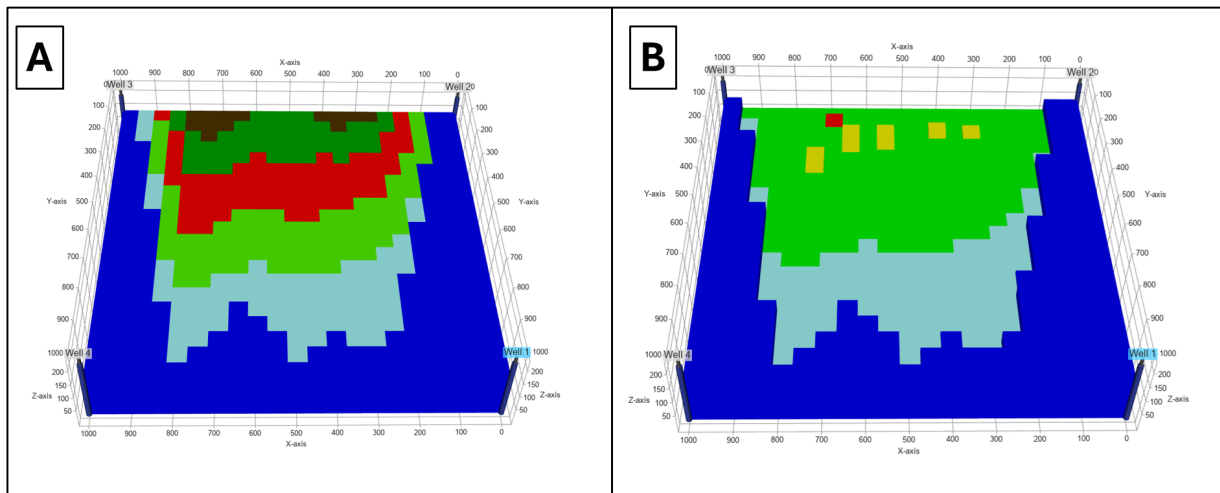
Figure 6.6: RRM models in flow diagnostic display with a resolution of 21 x 21 x 21, A: the full layers are displayed and B: part of the layers are removed to illustrate the channels

In figure 6.7, the grid resolution is increased to 51 x 51 x 51. As the resolution increased, the geometry of the deltaic started to mimic the sketched model. However, the channels are still showing discontinuity. This discontinuity in the channels can create errors in the simulations as the CO_2 can be trapped within these patchy layers of the channels. For that, grid resolutions of 51 x 51 x 51 are not sufficient and need to be higher.
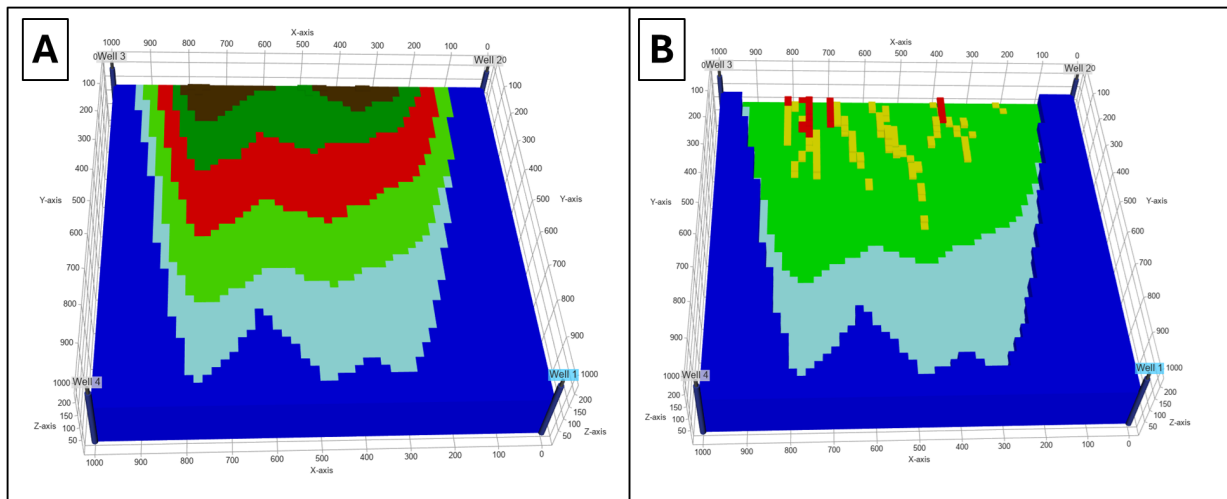
Figure 6.7: RRM models in flow diagnostic display with a resolution of 51 x 51 x 51, A: the full layers are displayed and B: part of the layers are removed to illustrate the channels

In figure 6.8, the grid resolution is increased to 81 x 81 x 81. With this resolution, the channels are fully captured with no discontinuity. In addition, the geometry of the deltaic layers is well defined, and patchy silty layers are captured as sketched. For that, this resolution will be used in the simulation phase.
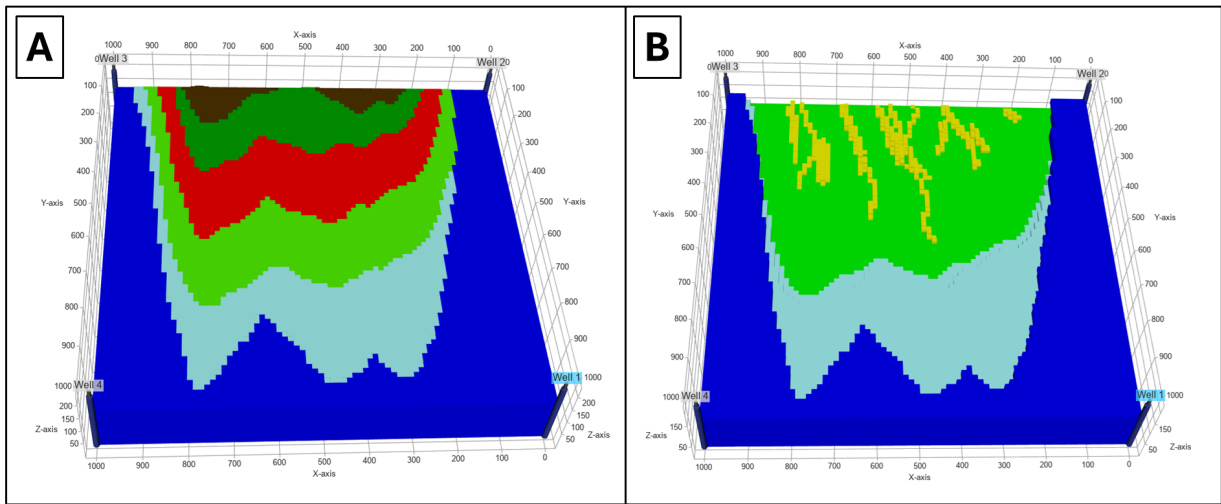
Figure 6.8: RRM models in flow diagnostic display with a resolution of 81 x 81 x 81, A: the full layers are displayed and B: part of the layers are removed to illustrate the channels

7

Dynamic Model

7.1. Well Placement

In the study, one injection well was used during the simulation, perforated in the bottom of the well within the reservoir sections. The location of the well was based on two main criteria. The first criteria, the well doesn't penetrate the impermeable layer as illustrated in figure 7.2. The second criteria, the location of the injector is in the middle of the reservoir to assure the injected CO_2 reaches all segments in the reservoir. The chosen location of the well is 41x51x81 as illustrated in figure 7.1.
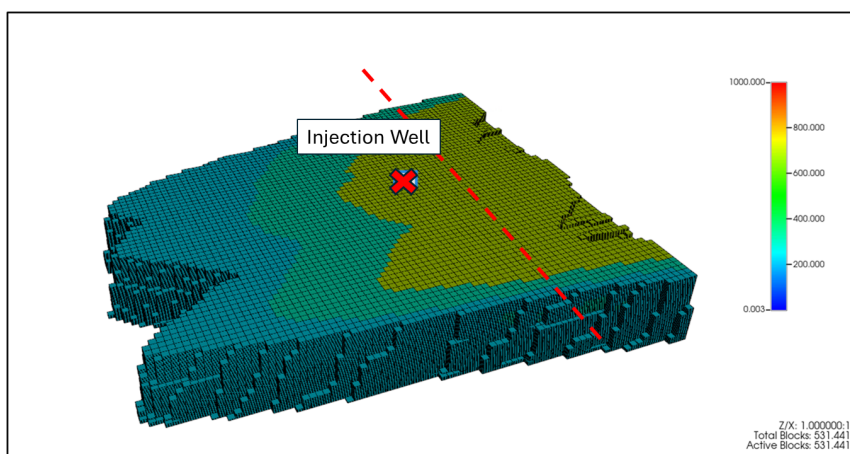
Figure 7.1: A 3D view for Model 4 showing the location of injection well. The color legend used for horizontal permeability "mD" for illustrations
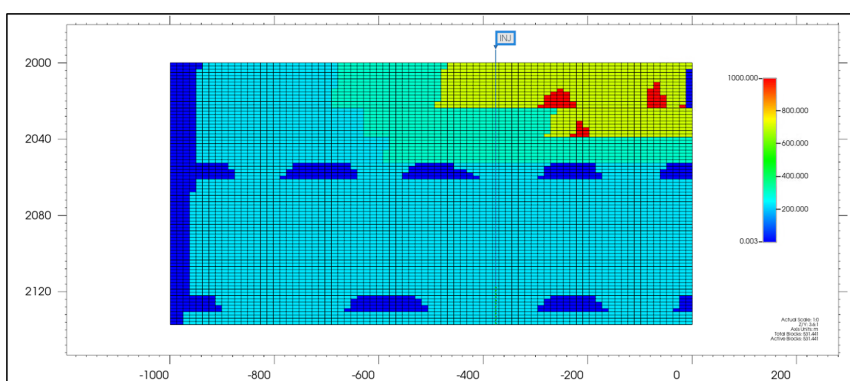
Figure 7.2: A cross-sectional view (Location of the cross-section indicated by a dashed line in figure 7.1) for Model 4 showing the location of the injection well. The color legend used for horizontal permeability "mD" for illustrations

7.2. Injection Rate:

The injection rate in this project is chosen to be 400 m^3/day as the reservoir gas rate for all realizations. The rate was chosen after several analyses and tests that evaluated the well performance during the 50 years of injections. The analysis was applied to all realizations but one model will be discussed in detail. Model 4 is chosen here as an example to illustrate the reasoning for choosing the injection rate at reservoir conditions. In model 4, 500 m^3/day reservoir injection rate was tested, resulting in reservoir pressure reaching the calculated operational reservoir pressure limit of 37000 kPa. Once the pressure of the reservoir reaches the limit after 39 years of injection, the reservoir injection rate starts to decrease significantly until it reaches 0 m^3/day after 45 years of injection. Figure 7.3 A, illustrates the drop in injection rate by a plot for model 4. The reason for dropping in pressure can be due to two main factors: rock compressibility or volume. The rock compressibility was adjusted (higher and lower) but still, a significant drop in the reservoir injection rate was observed. This concludes that the volume of the reservoir in this study is the reason for this critical drop and for that the bottom hole pressure and reservoir pressure difference are small leading to the critical drop in injection rate [43]. Figure 7.3 B illustrates the test using an injection rate of 400 m^3/day. The test with 400 m^3/day indicates no drop in injection rate and a stable increase of average reservoir pressure and well bottom-hole pressure with no drop. The analysis was applied to the other scenarios, Model 3 was similar to Model 4 as the average reservoir pressure reached maximum in the year 2065, and the injection rate reached zero in the year 2066. For Model 2 and Base Model, the average reservoir pressure was very close to the reservoir limit but it didn't face and drop in the injection rate (results included in the appendix). For that, the injection rate used for all models is 400 m^3/day to avoid the drop in injection rate and maintain a safe operation for all scenarios.
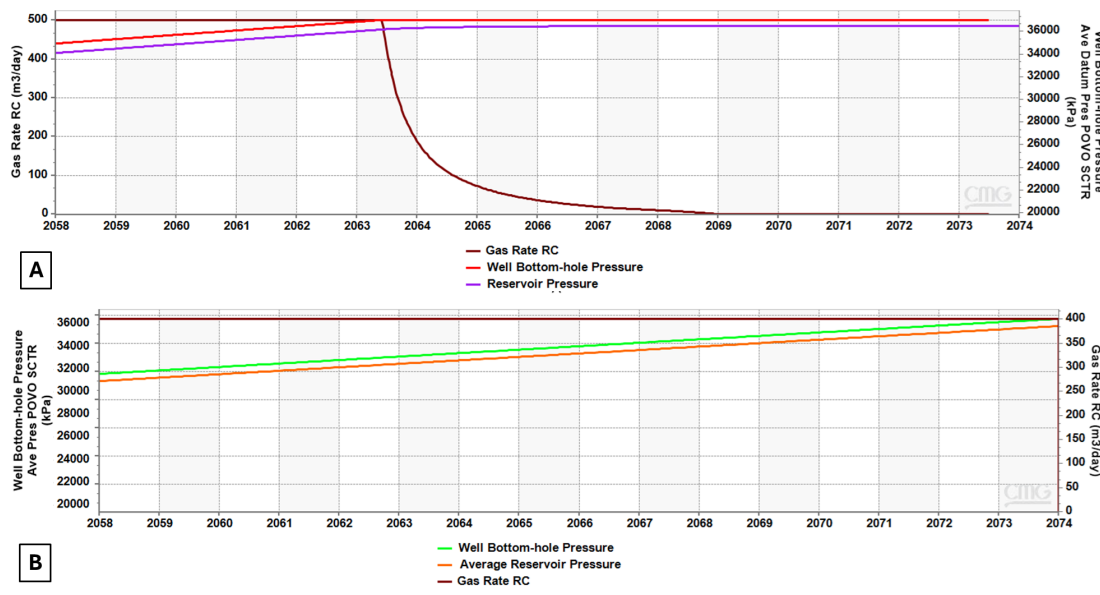
Figure 7.3: A plot for a test run. A: A run with using 500 m^3/day as gas injection rate at reservoir condition for Model 4. B: A run with using 400 m^3/day as the gas injection rate at reservoir condition for Model 4. The y-axises are the gas rate at reservoir condition and well bottom-hole pressure. X-axis is the period time (unit: years)

7.3. Base Model

The base model represents the realization with high petrophysical properties and continuous impermeable layer as illustrated in figure 6.3 and table 6.1. Figure 7.4 illustrates the CO_2 plume migration within 100 years, 50 years of CO_2 injection, and 50 years of monitoring (injection operations ended in the year 2074). In year one, three plume movements vertically due to buoyance effects are observed, the formation of three plumes within the reservoir indicates the the effect of the two impermeable layers. The thicknesses of layers between the impermeable layers control the plume distribution as the deepest plume and shallowest

plumes reach the impermeable layers and start to distribute laterally. Between 10 and 20 years, all three plumes reach the impermeable layers and start to distribute laterally, especially in higher porosity and permeability layers. After 50 years (the injecting well is shut-in), the plumes reach the maximum lateral distribution from the injection point. The saturation of CO_2 is observed in the most shallow plume and the lowest saturation in the deepest plume within the reservoir. After the injecting well is shut-in, CO_2 saturation near and at the injection point decreases significantly and the CO_2 plumes expand within the reservoir but remain confined within the impermeable layers. The spreading of CO_2 plumes is more observable after the injection in the upper and middle layers and less affected in the lower CO_2 plume.

Figure 7.5 illustrates two plots: A and B. For Figure A, three lines are displayed for Well bottom-hole pressure, Gas rate in surface condition, and average reservoir pressure. A slight variation between the bottom-hole pressure and average reservoir pressure is observed in Figure A, where the bottom-hole pressure is slightly higher. The variation between both lines remained constant for 100 years. The average reservoir pressure started around 21000 kPa and increased gradually reaching less than 32000 kPa at the end of the injection phase (2074), the reservoir limit is 37000 kPa. After the year 2074, both pressures remained constant as no injection activity was applied. The gas rate at surface condition started at 17000 m^3/day and increased gradually to 19000 m^3/day in 2074 and then dropped to zero m^3/day as the well was shut-in. Figure B indicates the cumulative amount of trapped CO_2 in the reservoir. In CMG simulation, trapped $CO2$ refers to the volume of $CO2$ that remains immobilized within the reservoir due to different trapping mechanisms. It starts at zero mol in 2024 and increases steadily reaching 66 billion mol in 2124, which is equal to 3 million tonnes of CO_2 within the 100 years of operation and monitoring. The amount of CO_2 in the yearly base can be calculated to be 60000 tonnes of CO_2 in the base model scenario. In addition, the CO_2 trapped plot shows peaks and sudden changes observed between the years 2029 to 2049 and in the year 2074.

Figure 7.4: CO_2 saturation in Base Model reservoir inspired by Sobrarbe Deltaic Complex outcrop over 100 years

Figure 7.5: Group plots for Base Model results. A: Well bottom-hole pressure, gas rate in surface condition, and average reservoir pressure over 100 years (2074 is the year of stopping injection)

7.4. Model 2

Model 2 represents the realization with high petrophysical properties and patchy impermeable layers as illustrated in figure 6.4 and table 6.1. Figure 7.6 illustrates the CO_2 plume migration within 50 years of CO_2 injection and 50 years of monitoring. In year one, the CO_2 plume is primarily concentrated near the injection well and distributed in a narrow vertical shape. Between 10 years to 20 years, the plume migrated vertically and laterally due to the buoyancy effect. The patchy impermeable layer begins to affect the CO_2 distribution, causing the plume to spread laterally below the impermeable layer. However, the vertical migration continues around the impermeable layer until it reaches the top of the reservoir where it starts to create the major plume in the reservoir by distributing laterally and vertically. At the end of the injection period (2074), the plume concentrated heavily at the top of the reservoir with minor plumes creating around the patchy impermeable layers. After the injection phase, the CO_2 plume is stabilized, and the main plume is still trapped at the top of the reservoir. However, the minor plumes are still trapped below the impermeable layer. In addition, changes in CO_2 saturations were observed after the injection phase which will be discussed in the discussion section.

Figure 7.7 illustrates two main plots: A and B for Model 2. In Figure A, the average reservoir pressure is slightly lower than the well bottom-hole pressure in all periods of injection and monitoring. The average reservoir pressure started around 21000 kPa and increased gradually reaching more than 33000 kPa at the end of the injection phase and then became constant until 2124. The gas rate at the surface condition trend is similar to the trend in the base model, where it starts at 17000 m^3/day to 19000 m^3/day at the end of the injection phase. Figure B illustrates the cumulative amount of trapped CO_2 in the Model 2 reservoirs. The plot shows an increase in CO_2 mol reaching 55 billion mol in 2124, equal to 2.5 million tonnes of CO_2 within the the whole period of operation and monitoring. The yearly amount of trapped CO_2 is 48000 tonnes of CO_2 in the Model 2 scenario. In addition, the plot of CO_2 trapped illustrates peaks and sudden changes that will be discussed in the discussion section.
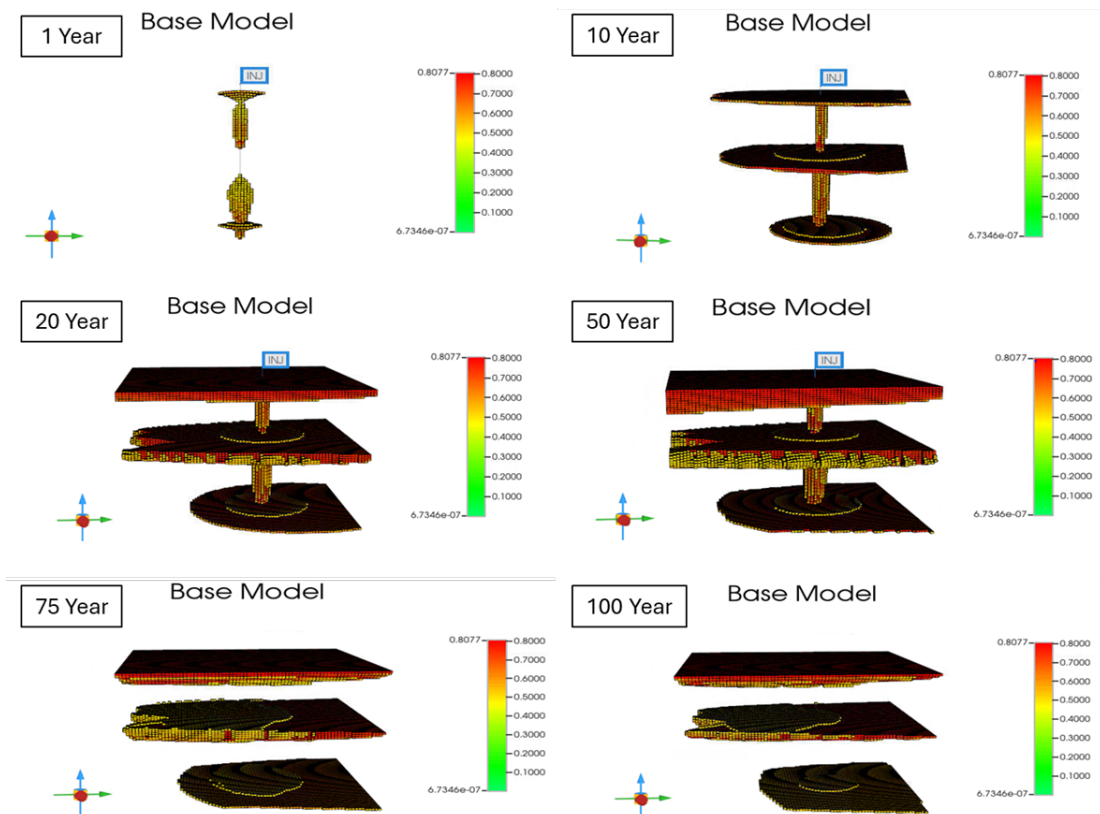
Figure 7.6: CO_2 saturation in Model 2 reservoir inspired by Sobrarbe Deltaic Complex outcrop over 100 years

Figure 7.7: Group plots for Model 2 results. A: Well bottom-hole pressure, gas rate in surface condition, and average reservoir pressure over 100 years (2074 is the year of stopping injection)

7.5. Model 3

Model 3 represents the realization with low petrophysical properties and continuous impermeable layers as illustrated in figure 6.3 and table 6.1. Figure 7.8 illustrates the CO_2 plume migration within 100 years including 50 years of CO_2 injection and 50 years of monitoring. In year one, three plumes started to vertically migrate bounded by two impermeable layers and the top of the reservoir. The deepest plume represented by the thinnest layer capped by an impermeable layer is the only plume that started to distribute

laterally. Between 10 years to 20 years, all plumes started to be distributed laterally and vertically due to the buoyancy effect. In the beginning, the plume in the middle was the most plume that migrated laterally but then the shallowest plume became more laterally distributed. However, comparing the plume migration from Model 3 with the Base model, it's clear that due to lower petrophysical properties, the saturation and distribution of the plumes are less in Model 3. At year 50, the plumes reached the maximum distribution and saturation of CO_2. The most lateral migrated plume is the shallowest plume in the reservoir and the lowest lateral migrated plume is the deepest plume in Model 3. After the injection period (2074), the CO_2 saturation decreased at the well point but with more stability of CO_2 plumes within the reservoirs.

Figure 7.9 illustrates the two plots: A and B. In Figure A, similar to previous models, the pressure difference between the well bottom-hole pressure and average reservoir pressure is slight with average reservoir pressure being less than the well bottom-hole pressure. Both start from around 21000 kPa and increase with a linear trend reaching 35500 kPa at the end of the injection phase. Comparing the average reservoir pressure in Model 3 with the previous models, Model 3 shows higher reservoir pressure and getting close to the reservoir limit, which is 37000 kPa. After the year 2074, the injection well was shut-in and the pressure of the reservoir remained constant. The gas rate at the surface condition starts at 17000 m^3/day and reaches 19500 m^3/day after 50 years and drops to zero m^3/day after shut-in the well, which is slightly higher than the result in the Base Model. In Figure B, the cumulative amount of trapped CO_2 in the Model 3 reservoir. Similar to the previous results, the trapped CO_2 starts to increase gradually with sudden changes mainly in the year 2074 and year 2029. In the year 2124, the estimated cumulative trapped CO_2 is estimated to be 5.2 billion mol of CO_2, which is equal to 2.3 million tonnes of CO_2. The amount of trapped CO_2 per year is calculated to be 46000 tonnes trapped in the reservoir.

Figure 7.8: CO_2 saturation in Model 3 reservoir inspired by Sobrarbe Deltaic Complex outcrop over 100 years
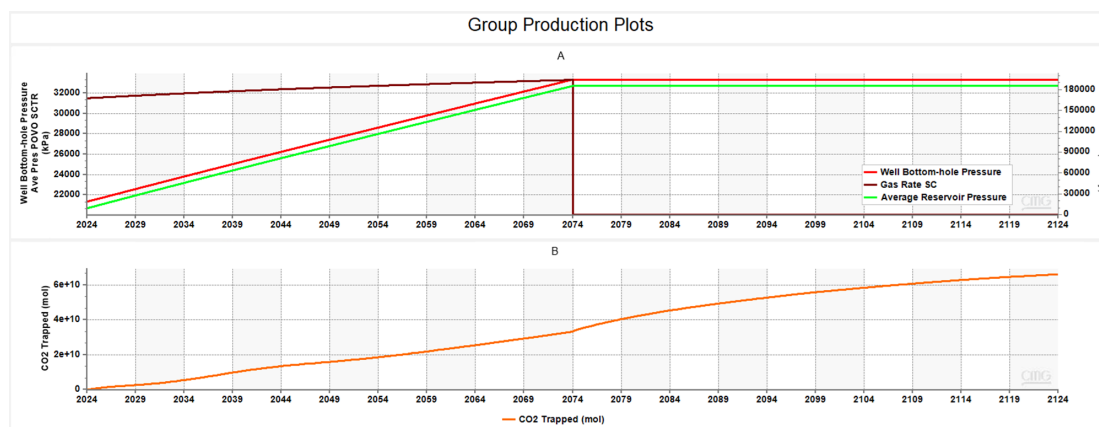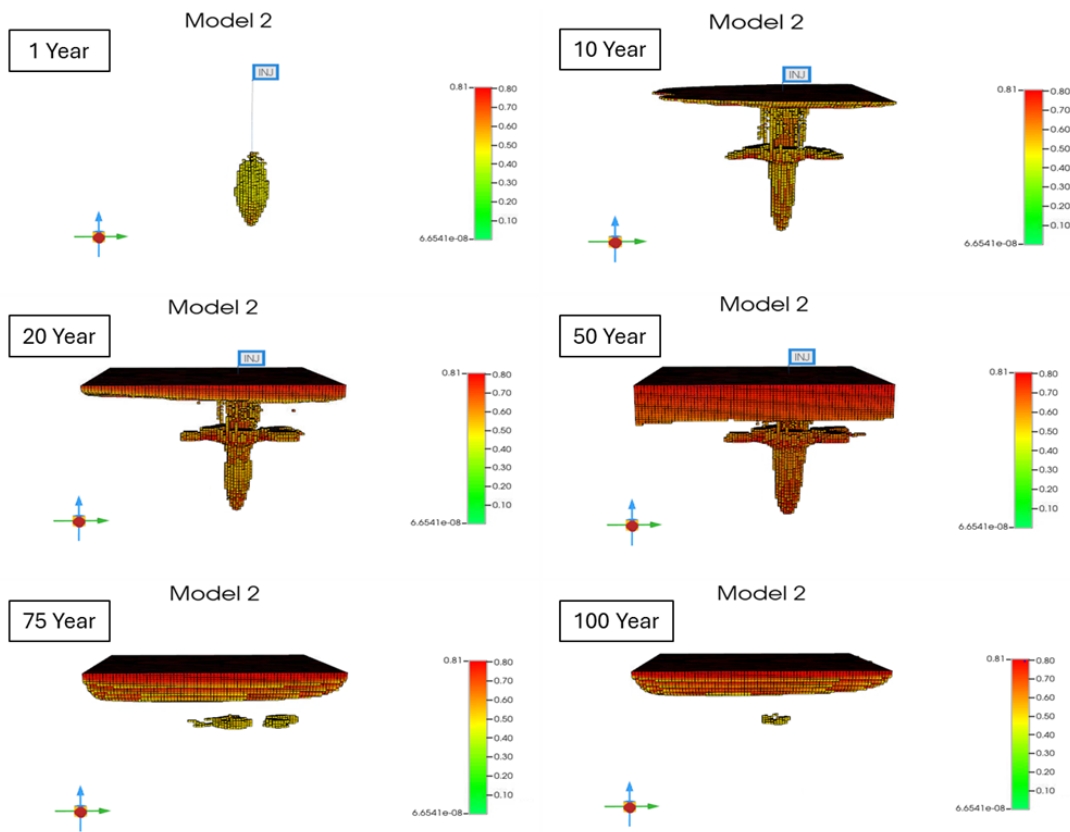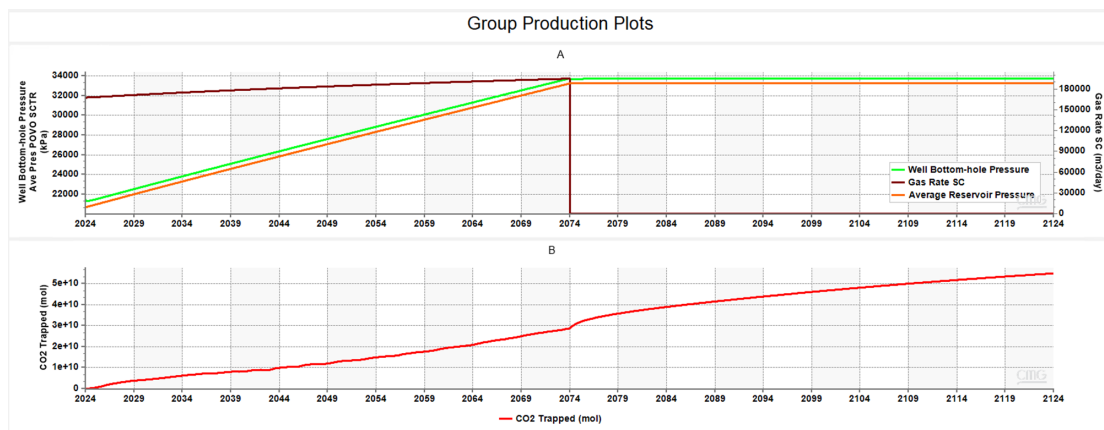
Figure 7.9: Group plots for Model 3 results. A: Well bottom-hole pressure, gas rate in surface condition, and average reservoir pressure over 100 years (2074 is the year of stopping injection)

7.6. Model 4

Model 4 represents the realization with low petrophysical properties and patchy impermeable layers as illustrated in figure 6.4 and table 6.1. Figure 7.10 illustrates the CO_2 plume migration within 50 years of CO_2 injection then 50 years of monitoring. In the first year, the CO_2 plume started to migrate vertically near the injection well, the migration of the plume is slower than the first year result in Model 2 which led to slightly higher lateral distribution but lower vertical migration compared to Model 2. Between 10 years and 20 years, the plume migrated vertically due to the buoyancy effect until it hit the patchy impermeable layer. Once it hit the impermeable layer, the CO_2 plume started to migrate laterally blow the impermeable layer. Compared to Model 2, the plume saturation below the impermeable layer is much less in Model 4 compared to Model 2 scenario. However, the vertical migration of the plume continues until it reaches the top of the reservoir where it starts to create the main plume with the clear lateral distribution. The maximum distribution of the plume in Model 4 is observed in the year 2074 representing the end of the injection phase. After the injection phase, the CO_2 major plume is more stabilized, while the minor plume is more distributed laterally but with significantly less saturation. Compared with Model 2, the minor plumes in Model 2 are less distributed laterally but with more saturation mainly near the injection point, whereas in Model 4 the saturation is critically less but with more lateral distribution. In addition, the CO_2 gas saturation, in general, is significantly less compared with Model 2, represented with the domination of yellow color in Model 4 (legend of CO_2 saturation is illustrated in Figure 7.10.

Two plots are displayed in figure 7.11. Figure A, the trend of average reservoir pressure and well bottom-hole pressure observed in the previous models are similar to the results in Model 4. However, the average reservoir pressure started around 21000 kPa and increased reaching approximately 36000 kPa at the end of the injection phase (2074), which is close to the reservoir pressure limit (37000 kPa). The observed trend of average reservoir pressure in Model 4 is the highest compared to previous results. The gas rate at the surface condition trend starts at 17000 m^3/day reaching 20000 m^3/day at the end of the injection phase, then dropping to zero m^3/day as the injection well is shut-in. In Figure B, the cumulative trapped CO_2 reaches 50 billion mol in ear 2124, equal to 2.2 million tonnes of CO_2. The amount of trapped CO_2 per year is calculated to be 44000 tonnes of trapped CO_2 in the reservoir.
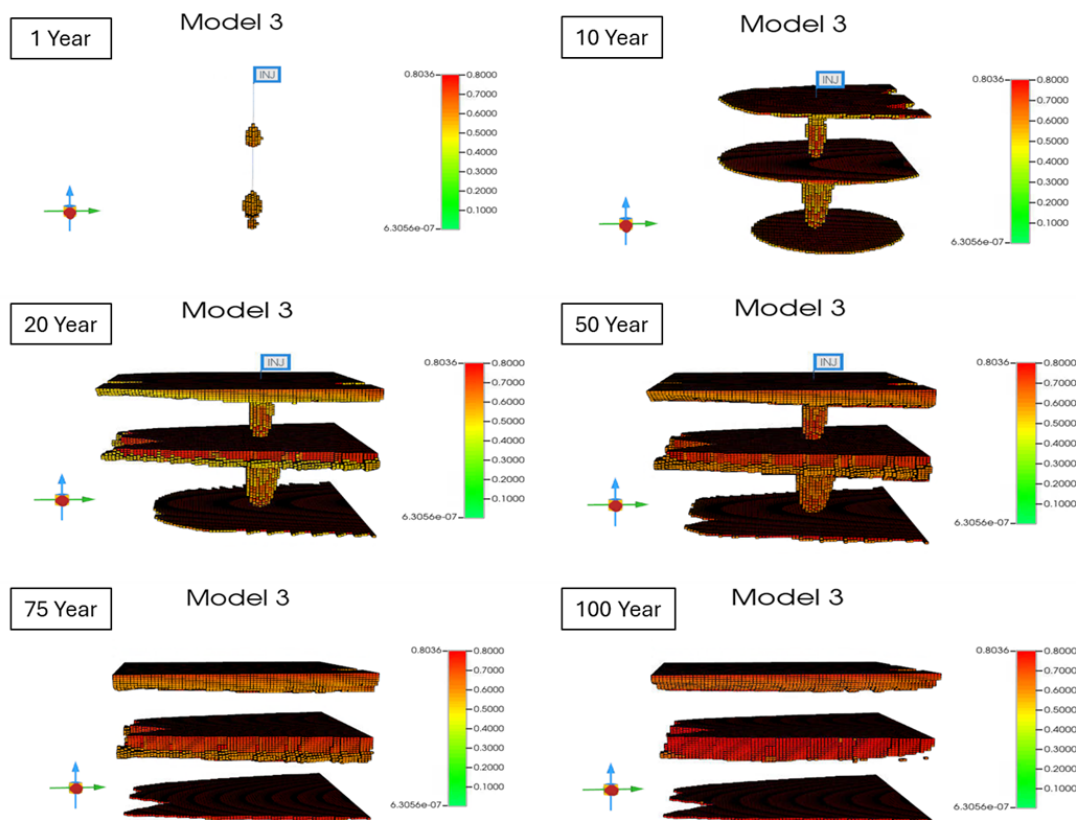
Figure 7.10: CO_2 saturation in Model 4 reservoir inspired by Sobrarbe Deltaic Complex outcrop over 100 years
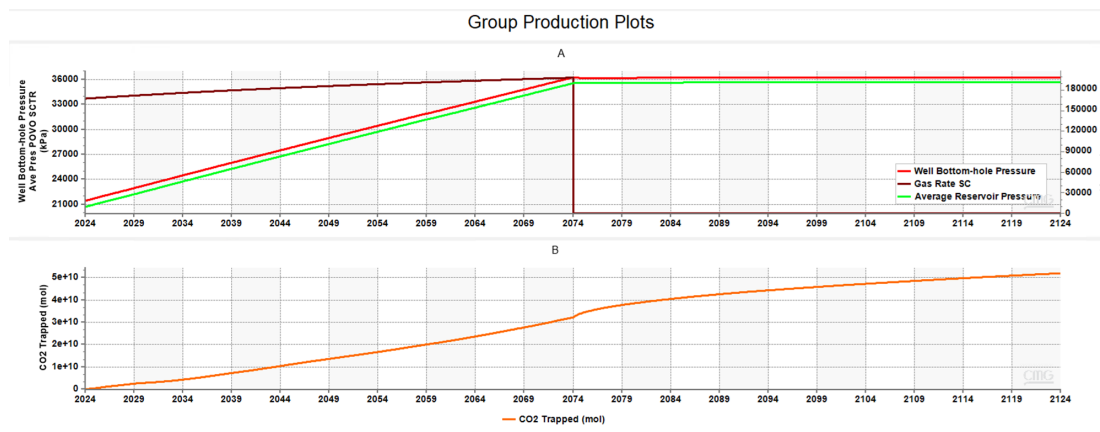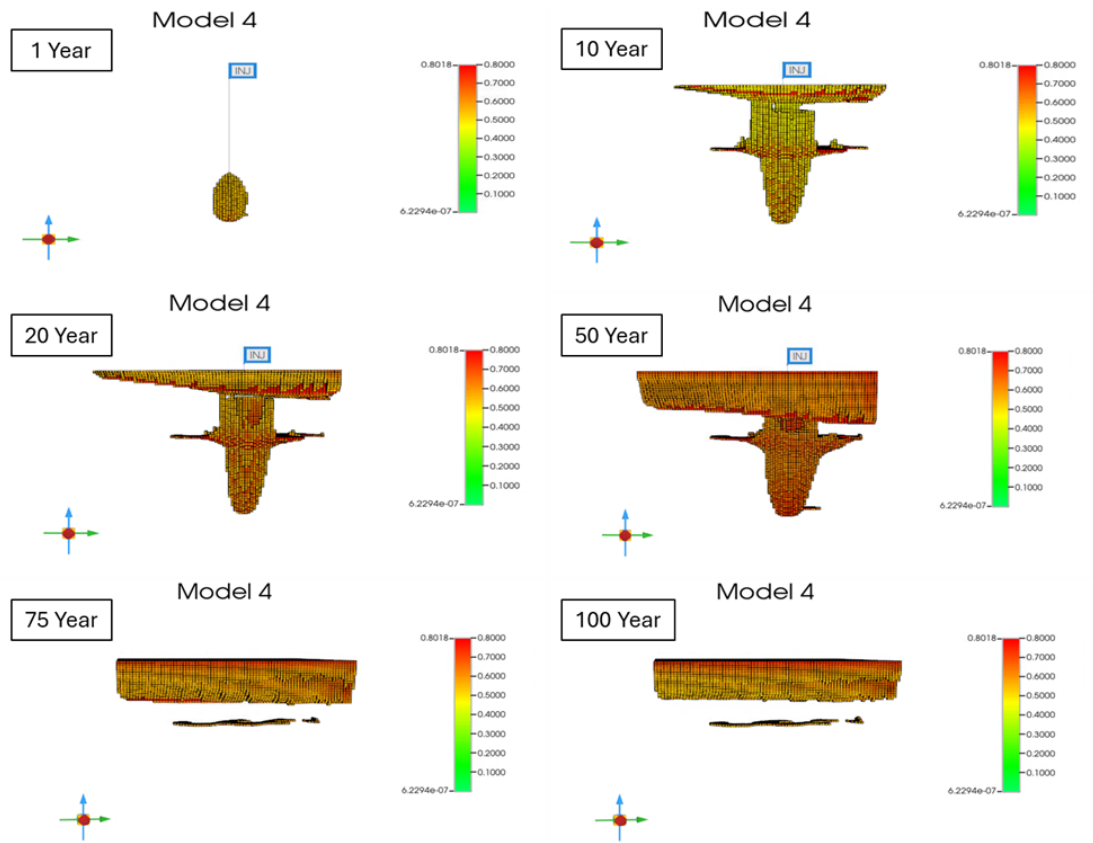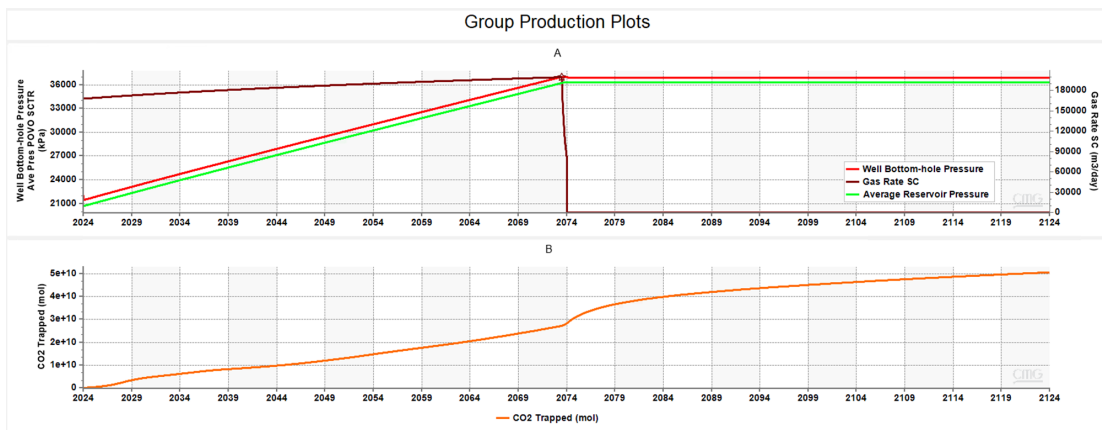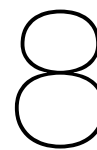

Figure 7.11: Group plots for Model 4 results. A: Well bottom-hole pressure, gas rate in surface condition, and average reservoir pressure over 100 years (2074 is the year of stopping injection)

8

Discussion

The results of the four realizations are analyzed and discussed in this chapter. The models are summarized in table 6.1, Base Model and Model 3 characterized by continuous impermeable layers. While Model 2 and Model 4 represent the models with patchy impermeable layers. For the petrophysical aspects, Base Model and Model 2 considered high values for porosity and permeability. Meanwhile, Model 3 and Model 4 consider low porosity and permeability values relatively.

8.1. Plume Migration:

The plume migration in the four scenarios was analyzed in reservoir conditions. The buoyancy effect is the main driving factor in migrating the plume vertically.

The lateral migration of CO_2 is primarily driven by the viscous forces generated by the high injection pressure starting at the wellbore and spreading away from the well. It is further influenced by pressure gradients allowing the CO_2 to spread through high-permeability layers. However, between models with continuous impermeable layers (Base Model and Model 3) and models with patchy impermeable layers (Model 2 and Model 4), the models with the continuous impermeable layers led to compartmentalizing the reservoir. The compartmentalization allowed the development of three CO_2 plumes, the plume's lateral and vertical distributions were controlled by the thickness of the layers and petrophysical properties. The deepest plume in Base Model and Model 3 is the first plume to hit the impermeable layer allowing for lateral migration before the other plumes. However, the influence in terms of plume development of the deepest plume is much less as the thickness is thinner compared to the middle and top compartments.

In the patchy impermeable layers scenarios (Model 2 and Model 4), the deepest impermeable layer did not trap the CO_2 and the plume continued the upward migration. This can be due to two factors; the well placement that avoided any contact with silty deposits and the larger space between the patchy silty deposits. Both factors allowed for plume vertical migration easily. The shallowest patchy impermeable layer has a major influence on the plume migration. Although the CO_2 plume migrated vertically to the top of the reservoir in these models, there are noticeable amounts of CO_2 accumulated locally below the patchy impermeable layers. At these localized plumes, there is observable upward escaping of the CO_2 at the edges of the silty patchy deposits due to the overfilling below the patchy silty layers. After the injection phase, the major CO_2 plume was concentrated in the top of the reservoirs as it stabilized with time until the end of the monitoring phase as the top of the reservoir was bounded by a seal.

Two models (Base Model and Model 2) represent high porosity and permeability scenarios and two models (Model 3 and Model 4) represent low porosity and permeability values scenarios. The main significant difference is the vertical migration shape of the CO_2 plume. In Base Model and Model 2, the shape of vertical migration is characterized by less lateral spreading due to higher permeability and porosity values. Due to the narrower shape of the vertical aspect of the plume, the major plumes in these models are more laterally distributed and in the case of patchy impermeable layers, more CO_2 are trapped below the patchy impermeable deposits. In Model 3 and Model 4, wider vertical distribution of the CO_2 plume led to less lateral distribution of the CO_2 plumes. The variations in shapes of the vertical migration are due to the following reasons: First, high porosity allows for more void spaces for CO_2 to occupy with less resistance and more evenly distributed. Second, higher permeability caused by better connectivity of the porous spaces in the reservoir leads to easier pathways.

The plume migration in all models reached the boundaries of the reservoir. As the boundary condition is closed, the flow cannot follow out of the reservoir leading to pressure build-up, and the shape of the plumes is artificially constrained by the shape of the reservoir.

8.2. Injection Rates and Reservoir Pressure:

With a fixed rate of CO_2 injection at reservoir condition (400 m^3/day), the average reservoir pressure was analyzed in all realization. Table 8.1, summarizes the average reservoir pressure at the end of the injection phase. The scenario of continuous impermeable layers resulted in less reservoir pressure compared to the patchy impermeable layers scenarios. However, the critical factor in the average reservoir pressure analysis is changes in petrophysical properties between the models. The high porosity and permeability values scenarios show significantly less average reservoir pressure at the end injection phase compared to the scenarios with low porosity and permeability values. For that, Model 4 with patchy impermeable layers and low porosity and permeability scenario is considered the scenario with the highest risk of exceeding the fracture pressure as it gets close to the reservoir limit pressure (37000 kPa). While the Base Model is the scenario with the lowest risk since the pressure is lower.

# of Models	Silty Layers Scenario	Petrophysical Scenario	Average Reservoir Pressure in Year 2074 [kPa]
Base Model	Continuous	High Scenario	32,700
Model 2	Patchy	High Scenario	33,226
Model 3	Continuous	Low Scenario	35,559
Model 4	Patchy	Low Scenario	36,271

Table 8.1: Comparison of different models realizations concerning average reservoir pressure in the year of 2074 "shut-in the injection"

8.3. Trapped CO_2:

In this section, the plots of trapped CO_2 for all realizations will be discussed. The results were introduced in the following figures from Base Model to Model 4 as the following: Figure 7.5, Figure 7.7, Figure 7.9, and Figure 7.11. The main observation from the plots is changes in the trends of trapped CO_2 specifically in the first years of operations. In the early years, the trend of trapped CO_2 increases gradually, which then transitions into a steeper incline as the trend accelerates. This increase in the trend of trapping CO_2 correlates with the plume reaching impermeable layers or the cap of the reservoir, where the CO_2 starts to be trapped by structural and stratigraphic mechanisms. In models with patchy impermeable layers (Model 2 and Model 4), the change in trend of trapping CO_2 is significantly higher compared with the other models. In addition, in Model 2 (higher porosity and permeability values) the change in the trend is observed earlier than in Model 4 (lower porosity and permeability values). While in Continuous impermeable layers realizations (Base Model and Model 3), the observable changes in the trend of trapping CO_2 are not observed. However, slight changes in trend are observed within the first 20 years due to the development of three main plumes within the compartments of the reservoir. Similar to the previous models (Model 2 and Model 4) the changes in the trend are detected earlier in the Base Model (high porosity and permeability values) compared to Model 3 (low porosity and permeability values). For all model scenarios, the year 2074 (end of injection period) shows an increase in the trend of trapped CO_2. The reasons for the increase are correlated with the introduction of other trapping mechanisms such as solubility and residual trappings along with the structure and stratigraphic trapping mechanism. From the CO_2 saturation figures, specifically between 75 years and 100 years, the CO_2 saturation changes after stopping injection operation as CO_2 will continue migrating upward leading to a decrease in the CO_2 saturation at the deeper part of the reservoir and an increase of brine in the reservoir. This process leads to trapping CO_2 by capillary forces as residual trapping and CO_2 dissolve in brine as solubility trapping.

Table 8.2 summarizes the cumulative trapped CO_2 within all scenarios and table 8.3 summarizes the average annual amount of trapped CO_2 for all scenarios. The model with the highest trapped CO_2 is the Base Model. The Base Model represents the most heterogeneous reservoir with the highest porosity and permeability values, which led to the highest trapped CO_2 of 3 million tonnes within 100 years and an average of 60000 tonnes of trapped CO_2 annually. Model 4 is the scenario with the lowest cumulative trapped CO_2 with 2.2 million tonnes and an average of 44000 tonnes of CO_2 trapped annually. Model 2 and Model 3 show similar results with 2.5 million tonnes and 2.3 million tonnes of CO_2 trapped within 100 years, an average of 48000 tonnes and 46000 tonnes of CO_2 trapped annually.

For that, the Base Model shows the highest efficiency in accommodating CO_2 with the lowest average reservoir pressure and highest cumulative trapped CO_2. Model 4 shows the lowest efficiency in accommodating CO_2 with the highest average reservoir pressure and lowest cumulative trapped CO_2.

# of Models	Silty Layers Scenario	Petrophysical Scenario	Cumulative Trapped CO_2 [tonnes]
Base Model	Continuous	High Scenario	3 million
Model 2	Patchy	High Scenario	2.5 million
Model 3	Continuous	Low Scenario	2.3 million
Model 4	Patchy	Low Scenario	2.2 million

Table 8.2: Comparison of different models realizations concerning cumulative trapped CO_2

# of Models	Silty Layers Scenario	Petrophysical Scenario	Average Annual Amount [tonnes]
Base Model	Continuous	High Scenario	60000
Model 2	Patchy	High Scenario	48000
Model 3	Continuous	Low Scenario	46000
Model 4	Patchy	Low Scenario	44000

Table 8.3: Comparison of different models realizations concerning the average annual amount of trapped CO_2

8.4. Uncertainties

As the study focused on the impact of large-scale reservoir heterogeneity on CO_2 storing applications, several sources of uncertainty can impact the results and the interpretations. The main source of uncertainty is the geological models in this study only focus on large-scale heterogeneity as small-scale geological features are not considered which can change the results and interpretations. The uncertainties in the geological data analysis section include the interpreted surfaces using the satellite image that represents the lateral distribution of the facies/facies association and the link of the marked surfaces with the Mondot-1 core, which represents the vertical distributions of the facies/facies associations. The petrophysical properties are one of the main factors in the CO_2 injecting and storing process. As the petrophysical data was collected from several literature studies, it adds a source of uncertainty to the reservoir models. In the dynamic phase, three main sources of uncertainties can be mentioned. First, lack of experimental studying for the area of interest. Second, the injection well in this study considered only one will in the middle of the reservoir. Considering alternative analysis to the well placement and multiple injection wells will definitely mitigate uncertainty, which was constrained by the time limitations of this study. Third, the plume migrations are constrained by the shape of the reservoir with the closed boundary condition. Adding structural and geomechanical aspects will allow for a better understanding of the boundary condition to mitigate the uncertainty of the reservoir boundary.

9

Conclusion

Thy study provides an analysis of the impact of large-scale reservoir heterogeneity on CO_2 storage efficiency inspired by the Sobrarbe Deltaic Complex in Ainsa, Spain. The Sobrarbe Deltaic Complex includes three formations as the following: Sobrarbe Formation, Escanilla Formation, and San Vicente Formation. The Sobrarbe Deltaic Complex is outcropped on the western part of the Eocene Ainsa Basin.

The simulation results emphasize the critical role of reservoir architecture and petrophysical properties in enhancing the trapping mechanisms of CO_2 in the reservoir. The Base Model, which represents continuous impermeable layers and a high scenario of petrophysical properties, showed the highest CO_2 trapping capacity, storing around 3 billion kg of CO_2 over 100 years with one injection well. In contrast, models that assumed patchy impermeable layers were less effective in trapping CO_2 and exhibited higher reservoir pressure, which increased the risk of leakage.

These findings highlight the importance of understanding the reservoir architecture. Reservoir features such as the impermeable layers can help trap CO_2 more efficiently, making them crucial for successful storage projects. Future work may focus on monitoring CO_2 movement over longer periods and consider small-scale heterogeneity to improve the reliability of CO_2 storage predictions. By that, future projects can better understand how to make CO_2 storage more effective as a solution for reducing CO_2 emissions and protecting the environment.

References

[1] Saudi & Middle East Green Initiatives. *Reducing Carbon Emissions: Saudi Green Initiative Target*. `https://www.greeninitiatives.gov.sa/about-sgi/sgi-targets/reduce-carbon-emissions/`. Accessed: 2024-07-10. n.d.

[2] *Paris Agreement*. Accessed: 2024-07-17. 2015. URL: `https://unfccc.int/sites/default/files/english_paris_agreement.pdf`.

[3] G. Cosgrove et al. "Intra☐clinothem variability in sedimentary texture and process regime recorded down slope profiles". In: *Sedimentology* (2020). Accessed: 2024-07-10. URL: `https://onlinelibrary.wiley.com/doi/full/10.1111/sed.12648`.

[4] Francis Odonne et al. "Soft-sediment deformation from submarine sliding: Favourable conditions and triggering mechanisms in examples from the Eocene Sobrarbe delta (Ainsa, Spanish Pyrenees) and the mid-Cretaceous Ayabacas Formation (Andes of Peru)". In: *Sedimentary Geology* 235.3 (2011). Recognising triggers for soft-sediment deformation: Current understanding and future directions, pp. 234–248. DOI: `https://doi.org/10.1016/j.sedgeo.2010.09.013`. URL: `https://www.sciencedirect.com/science/article/pii/S0037073810002733`.

[5] B. Metz et al. *IPCC Special Report on Carbon Dioxide Capture and Storage*. Accessed: 2024-07-10. IPCC, July 2005. URL: `https://www.osti.gov/biblio/20740954`.

[6] Luqman Abidoye et al. "Geological Carbon Sequestration in the Context of Two-Phase Flow in Porous Media: A Review". In: *Critical Reviews in Environmental Science and Technology* 45 (Mar. 2015), pp. 1105–1147. DOI: `10.1080/10643389.2014.924184`.

[7] Jeremiah D. Moody. *Variations in the architecture of fluvial deposits within a marginal marine setting, Eocene Sobrarbe and Escanilla formations, Spain*. 2014. URL: `https://hdl.handle.net/11124/10608`.

[8] Dewey J.F. et al. "Kinematics of the western Mediterranean". In: *Geological Society, London, Special Publications* 45 (1989). DOI: `10.1144/gsl.sp.1989.045.01.15`.

[9] Meigs Andrew J. "Sequential development of selected pyrenean thrust faults". In: *Journal of Structural Geology* (1997). DOI: `10.1016/s0191-8141(96)00096-x`.

[10] Ingrid Anell et al. "A discourse on factors influencing the formation of sigmoidal and linear slope-geometries in the deltaic clinoforms of the calciclastic Sobrarbe Delta, Ainsa Basin, Spain". In: *Marine and Petroleum Geology* 153 (July 2023), p. 106287. DOI: `10.1016/j.marpetgeo.2023.106287`.

[11] Moss-Russell A. et al. "The stratigraphic architecture of a prograding shelf-margin delta in outcrop, the Sobrarbe Formation, Ainsa Basin, Spain". In: *AAPG Search and Discovery* (Jan. 2009).

[12] Philipp J. Wolpert et al. "Borehole-image-log characterization of deltaic deposits from a behind-outcrop well: Opportunities and limitations". In: *Journal of Sedimentary Research* 89.12 (Dec. 2019), pp. 1207–1230. DOI: `10.2110/jsr.2019.75`. eprint: `https://pubs.geoscienceworld.org/sepm/jsedres/article-pdf/89/12/1207/4914610/i1527-1404-89-12-1207.pdf`. URL: `https://doi.org/10.2110/jsr.2019.75`.

[13] Tom Dreyer et al. "Architecture of the tectonically influenced Sobrarbe deltaic complex in the Ainsa Basin, northern Spain". In: *Sedimentary Geology* 127.3 (1999), pp. 127–169. DOI: `https://doi.org/10.1016/S0037-0738(99)00056-1`. URL: `https://www.sciencedirect.com/science/article/pii/S0037073899000561`.

[14] John J. Millington et al. "The Charo/Arro canyon-mouth sheet system, south-central Pyrenees, Spain; a structurally influenced zone of sediment dispersal". In: *Journal of Sedimentary Research* 65.4b (Nov. 1995), pp. 443–454. DOI: `10.1306/D426827F-2B26-11D7-8648000102C1865D`. eprint: `https:`

//pubs.geoscienceworld.org/sepm/jsedres/article-pdf/65/4b/443/2811741/443.pdf. URL: https://doi.org/10.1306/D426827F-2B26-11D7-8648000102C1865D.

[15] Josep Muñoz. "Evolution of a continental collision belt: ECORS-Pyrenees crustal balanced cross-section". In: Jan. 1992, pp. 235–246. DOI: 10.1007/978-94-011-3066-0_21.

[16] E. REMACHA et al. *The Upper Hecho Group turbidites and their vertical evolution to deltas (Eocene, South-central Pyrenees) Excursion Guidebook, 15th International Sedimentological Congres, International Association of*. Jan. 1998.

[17] Pierre Labaume et al. "Megaturbidites: A depositional model from the eocene of the SW-Pyrenean Foreland basin, Spain". In: *Geo-Marine Letters* 7.2 (June 1987), pp. 91–101. DOI: 10.1007/BF02237988.

[18] M. Soler-Sampere et al. *Líneas generales de la geología del Alto Aragón Occidental*. 1970.

[19] Matthew Thomas Hall. "Sequence stratigraphy and early diagenesis: the Sobrarbe Formation, Ainsa Basin, Spain". PhD thesis. The University of Manchester, 1997.

[20] John D. Marshall et al. "The Mondot-1 Core, Aínsa Basin, Spanish Pyrenees: a deltaic reservoir teaching set with augmented reality". In: *Geological Society, London, Special Publications* 527.1 (2023), pp. 279–302. DOI: 10.1144/SP527-2022-6. eprint: https://www.lyellcollection.org/doi/pdf/10.1144/SP527-2022-6. URL: https://www.lyellcollection.org/doi/abs/10.1144/SP527-2022-6.

[21] Robert M. Mitchum et al. "High-frequency sequences and their stacking patterns: sequence-stratigraphic evidence of high-frequency eustatic cycles". In: *Sedimentary Geology* 70.2-4 (Mar. 1991), pp. 131–160. DOI: 10.1016/0037-0738(91)90139-5.

[22] Khalid Ubeid. "The Sobrarbe Delta (Eocene) on the Eastern Flank of the Santa María del Buil Syncline (Aínsa Basin, Central-Southern Pyrenees, Northern Spain): Facies, Architecture and their Relationship with Deep Marine Systems". English. Thesis directors: Luis Pedro Fernández (dir. thes.) PhD thesis. University of Oviedo, 2008. URL: https://www.educacion.gob.es/teseo/imprimirFicheroTesis.do?idFichero=Fxc3xwn4RqM%3D.

[23] S. Djin Nio et al. "Diagnostic Attributes of Clastic Tidal Deposits: A Review". In: 1991. URL: https://api.semanticscholar.org/CorpusID:130753924.

[24] Henri Sahat Mian Parulian Silalahi. *Stratigraphic architecture of slope deposits associated with prograding margins, Sobrarbe Formation: Ainsa Basin, Spain*. 2009. URL: http://hdl.handle.net/11124/170363.

[25] L. Becker et al. "Behind-the-Outcrop Research Drilling in the Sobrarbe Delta, Ainsa Basin: Core Description and Sedimentation Processes in a Mixed Carbonate-Siliciclastic Delta Complex". In: *Digital Geology: Multi-scale analysis of depositional systems and their subsurface workflows*. EAGE, Jan. 2020. DOI: 10.3997/book9789462823372. URL: https://doi.org/10.3997/book9789462823372.

[26] Google Earth. *Google Earth, version 7.3.3.7786*. Software. Available at: https://www.google.com/earth/. 2024.

[27] Achyut Mishra et al. "High Resolution Characterization of Lithological Heterogeneity of the Paaratte Formation, Otway Basin (Australia), a Coastal to Shallow-Marine Deposit". In: *Geosciences* 9 (June 2019), p. 278. DOI: 10.3390/geosciences9060278.

[28] Huaye Liu. "Fluvial-delta Sand Types and Its Controling Reservoir Effection of the Second and Third Members". In: *IOP Conference Series: Materials Science and Engineering* 585 (Aug. 2019), p. 012085. DOI: 10.1088/1757-899X/585/1/012085.

[29] S. S. Selim et al. "Sedimentology and reservoir characteristics of delta plain reservoirs: An example from Messinian Abu Madi Formation, Nile Delta". In: *Marine and Petroleum Geology* 139, 105623 (Jan. 2022), p. 105623. DOI: 10.1016/j.marpetgeo.2022.105623.

[30] Shiyue Fang et al. "Fine log interpretation model of reservoir in Huatugou oilfield". In: (Jan. 2016). DOI: 10.2991/imst-16.2016.22.

[31]   Dr. Richmond Ideozu et al. *Controls of Depositional Environments on Reservoir Quality in Terms of Porosity and Permeability Gabo Field Niger Delta*. Apr. 2019. DOI: `10.20944/preprints201904. 0280.v1`.

[32]   Shengli Li et al. "Change of deltaic depositional environment and its impacts on reservoir properties—A braided delta in South China Sea". In: *Marine and Petroleum Geology* 58 (Dec. 2014), pp. 760–775. DOI: `10.1016/j.marpetgeo.2014.06.003`.

[33]   Allard Martinius. *An outcrop location of the boundary between two composite sequences (Comaron Compsite Sequence and Las Gorgas Composite Sequence)*. Personal communication. 2023.

[34]   Rapid Reservoir. *Rapid Reservoir Model*. Accessed: 2024-07-09. 2024. URL: `https://rapidreservoir. org/`.

[35]   Carl Jacquemyn et al. "Sketch-based interface and modelling of stratigraphy and structure in three dimensions". English. In: *Journal of the Geological Society* 178.4 (July 2021). DOI: `10.1144/jgs2020– 187`.

[36]   Shedid Shedid. "Vertical-horizontal permeability correlations using coring data". In: *Egyptian Journal of Petroleum* 28 (Mar. 2019). DOI: `10.1016/j.ejpe.2018.12.007`.

[37]   Cmgl.ca. *Introduction to CMG's Modeling Workflow*. PowerPoint presentation. 2022.

[38]   Schlumberger Oilfield Glossary. *Pressure Gradient*. Accessed: 2024-07-31. 2024. URL: `https: //glossary.slb.com/en/terms/p/pressure_gradient`.

[39]   Peace Software. *CO2 Properties Calculator*. Accessed: 2024-08-26. URL: `https://www.peacesoftware. de/einigewerte/co2_e.html`.

[40]   University of British Columbia. *Density of Rocks and Minerals*. Accessed: 2024-08-26. URL: `https: //www.eoas.ubc.ca/courses/eosc350/content/foundations/properties/density.htm`.

[41]   Leon Gutierrez. *Hysteresis in Porous Media: The Land Model*. Accessed: 2024-08-26. 2007. URL: `https://diamhomes.ewi.tudelft.nl/~kvuik/numanal/gutierrez_scriptie.pdf`.

[42]   Gloria López. "Walther's Law of Facies". In: June 2015, pp. 957–958. DOI: `10.1007/978–94–007– 6304–3_30`.

[43]   Gemma Jones. *Significnt drop in injection rate after reservoir pressure reaching to the limit*. Personal communication. 2024.

A
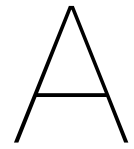
Appendix

Facies/FA	Porosity	Permeability
Delta Front	28.4	182
	14.1	
	17.2	
	21.5	
	21.5	
	16.3	
	27.6	268
	25	520
	25	141
Mouthbar	31	4930
	30	1010
	23	10300
	28	2040
	30	1820
	27	407
	28	1190

Table A.1: All gathered porosity and permeability data from literature

Facies/FA	Porosity	Permeability
Channel	29	318
	29	535
	29	378
	29	380
	26.9	7410
	29	2810
	39	747
	30	1140
	28	1110
Siltstone	0.21	0.003
	0.16	
Prodelta	1	0.8
	3	10
Upper Delta Plain	4	0.7
	30	1225
Lower Delta Plain	24	800
	30	850
	29	270

Table A.2: All gathered porosity and permeability data from literature
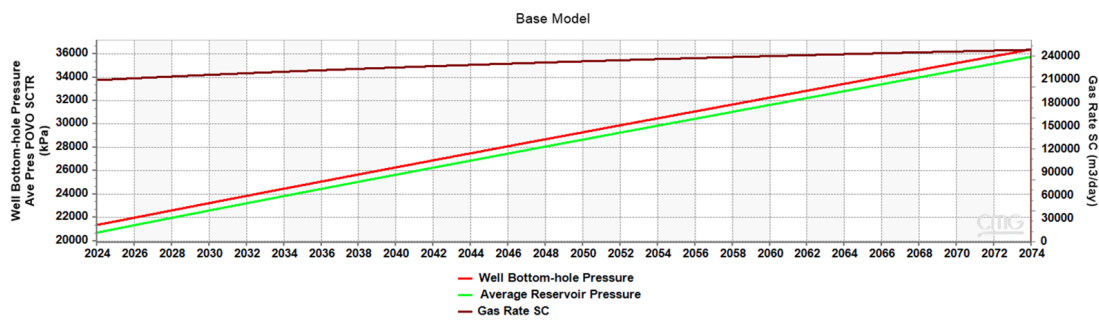
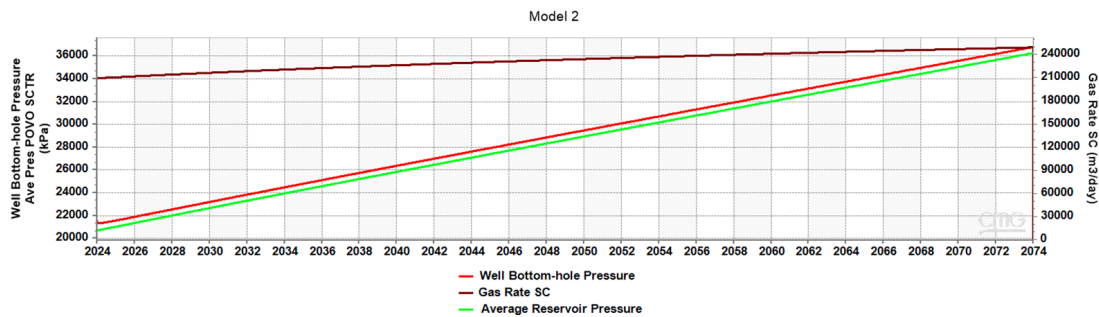**Figure A.1:** A plot for Base Model with an injection rate of 500 m^3/day

Figure A.2: A plot for Model 2 with an injection rate of 500 m^3/day
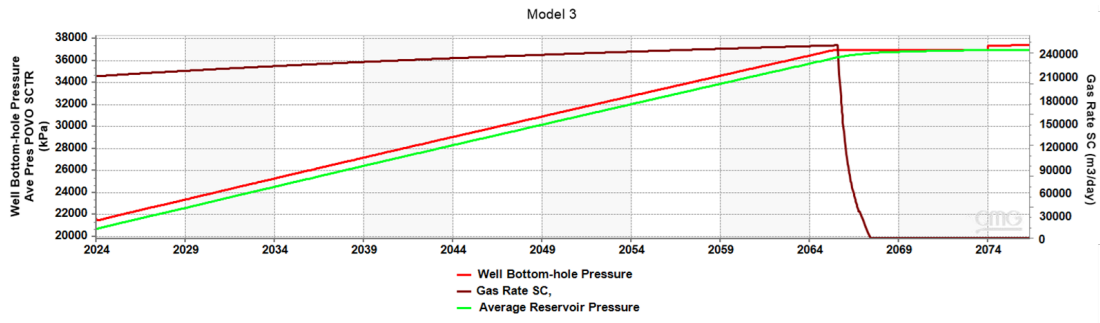
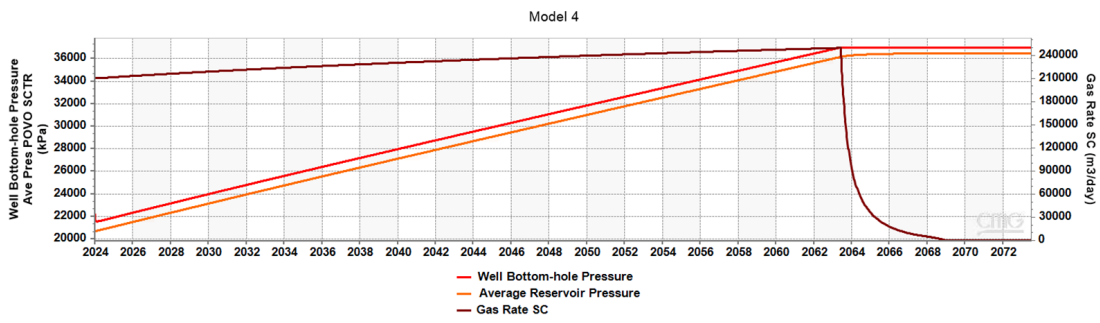**Figure A.3:** A plot for Model 3 with an injection rate of 500 m^3/day

Figure A.4: A plot for Model 4 with an injection rate of 500 m^3/day